

Performance and characterization of nano-engineered silica waste concrete composite for efficient marine radionuclides remediation

Jean-Baptiste Mawulé Dassekpo^{a,*}, Chonkei Iong^b, Dejing Chen^b,
Feng-liang Zhang^b, Xiaoxiong Zha^b, Jianqiao Ye^{c,*}

^a Institute of Technology for Marine Civil Engineering, Shenzhen Institute of Information Technology, 518172, PR. China

^b School of Civil and Environmental Engineering, Harbin Institute of Technology, Shenzhen, 518055, China

^c School of Engineering, Lancaster University, Lancaster LA1 4YR, UK

*Corresponding authors email: dassekpo.jb@szit.edu.cn, j.ye2@lancaster.ac.uk

Abstract

The disposal of solid and radioactive waste poses significant risks to terrestrial and marine ecosystems. This study presents a sustainable solution by recycling silica-rich glass waste (RG) and fly ash (FA) to develop a functional nanocomposite concrete for radionuclide treatment. A Radionuclide removal Zeolite (RrZ) was hydrothermally synthesized from RG powder at low temperature and NaOH molar ratio. The RrZ was incorporated into a porous geopolymer composite concrete (PGCC) comprising 20% RrZ and 80% FA, with $\text{SiO}_2/\text{Na}_2\text{O} = 1$, liquid-to-solid ratio (L/S) = 0.33, paste-to-bone ratio (B/A) varying from 0.15–0.2, and porosity (P) from 14.95–25.45%. The results from SEM, TEM and BET indicated a highly porous structure of RrZ adsorbent with mesopores capable of achieving high adsorption efficiency (83.13–97.71% for Sr^{2+} and 55.31–91.01% for Cs^+) within short time, adhering to the quasi-second-order kinetic models. Moreover, the XRD results identified key crystalline phase of analcime ($\text{NaAlSi}_2\text{O}_6 \cdot \text{H}_2\text{O}$), and no new phase formed after ion exchange with Sr^{2+} and Cs^+ , while the FTIR analysis revealed minimal chemical changes post-adsorption. Additionally, the porosity of 14.95% - 25.45% and water permeability of 1.876–11.956 mm/s were the key factors for PGCC design, while larger aggregates and lower B/A ratios helped to optimize the adsorption. The ANOVA analysis revealed that aggregate size was the most significant factor for single-cycle adsorption, followed by porosity and B/A ratio. This study demonstrates that PGCC effectively combines waste recycling with environmental remediation, offering a durable and efficient method for hazardous radionuclide removal from marine ecosystems.

Keywords: Waste glass, Fly ash, Adsorption kinetics, Nanocomposite concrete, Radionuclides treatment, Marine ecosystems.

1 **1. Introduction**

2 Environmental pollution, particularly the disposal of solid and radioactive waste, poses
3 significant risks to earth and marine ecosystems. Among various pollutants, radioactive
4 isotopes such as strontium (^{90}Sr) and cesium (^{137}Cs) are of concern due to their long half-lives
5 and bioaccumulation in marine organisms. Radionuclides can enter the marine environment
6 through discharges from nuclear power installations, nuclear accidents, and improper disposal
7 of nuclear waste, resulting in significant impacts on aquatic life and human health. With these
8 in mind, consider Japan's recent project to discharge over 1.3 million tons of nuclear
9 wastewater from the Fukushima Daiichi nuclear power plant into the Pacific Ocean, along with
10 past incidents like weapons testing and nuclear accidents, such as Chernobyl in 1986 and
11 Fukushima in 2011 and the accidental shutdown of the reactor occurred at Three Mile Island
12 nuclear power plant in the U.S. in 1979 [1-6]. These incidents released vast amounts of
13 radioactive materials into the environment, increasing an urgent need for its remediation.
14 Radionuclide contaminants are present in both natural and man-made environments [7], and
15 once found in the environment, undoubtedly becoming a major risk of transmission to humans,
16 affecting metabolic processes [8] and causing population health disorders [9]. In particular, the
17 impact of Sr and Cs contamination in marine ecosystems is profound. Both isotopes mimic
18 essential elements like calcium and potassium, allowing them to be absorbed by marine
19 organisms and enter the food chain. Over time, this contamination can affect biodiversity,
20 disrupt ecological balance, and increase radiation exposure to humans through seafood
21 consumption. The degree of radiation and toxicity of radioactive elements or its derived
22 byproducts are also a source of contamination for humans and ecosystems. Most radioactive
23 elements emit one or more types of radiation—alpha, beta, or gamma rays—from their unstable
24 nuclei, known as radionuclides. Alpha rays consist of positively charged helium atoms, while
25 beta rays are negatively charged electrons, and gamma rays are neutral electromagnetic
26 radiation with shorter wavelengths than X-rays. These short-wavelength, high-energy
27 radiations can penetrate and damage living tissue over short distances by breaking chemical
28 bonds in cellular molecules, potentially leading to abnormal cell division [3, 10-13].

29
30 Resolving the issue of nuclear waste disposal is essential for ensuring the safe and
31 sustainable growth of nuclear energy [14]. Proper management of nuclear waste is essential
32 not only for environmental protection but also for public safety and the long-term viability of
33 the nuclear industry. Ensuring that these pollutants are disposed in a secure and efficient

1 manner will minimize potential risks, support global energy needs, and foster public trust in
2 nuclear technology. Advances in nuclear waste disposal technologies and policies will play a
3 critical role in shaping the future of nuclear energy as a reliable and clean energy source. Safe
4 discharge of liquid radioactive waste into the environment is a highly regulated process due to
5 its potential adverse impact to the environment and human health. Stringent standards are in
6 place to ensure that the release of such waste is managed carefully [15]. These included the
7 reduction of radioactive content by significantly reducing the concentration of radioactive
8 substances to the levels below the prescribed limits by the International Atomic Energy Agency
9 (IAEA) or national authorities. This technique often involves processes such as filtration,
10 chemical precipitation, ion exchange, or evaporation [13], which isolate and remove
11 radioactive isotopes. Besides radioactive substances, other toxic solutes (e.g., heavy metals,
12 organic pollutants) also need to be minimized. Chemical treatment, adsorption, and membrane
13 filtration are commonly used methods to achieve this. In this perspective, a range of traditional
14 and emerging technologies have been explored and implemented for the treatment of heavy
15 metals in wastewater [16-24], and the separation of radioactive elements in aqueous solutions
16 became possible [13, 14, 25-29]. Currently, adsorption is the primary method for treating and
17 purifying heavy metals [30] and radioactive elements, owing to their lower cost, easy and speed
18 of operation, and broad applicability [31-33]. However, identifying a promising adsorbent with
19 high adsorption capacity, rapid adsorption/desorption mechanism, and low energy
20 consumption is crucial to meet pilot and industrial-scale requirements. In addition to these
21 criteria, other important factors include long-term durability, cost-effectiveness, sustainability,
22 and environmental friendliness should be considered. Despite its advantages, adsorption
23 method faces challenges such as poor stability, selectivity, and limited adsorption capacity [13,
24 14]. Hence, the design and preparation of high-performance adsorbents capable of efficiently
25 treating radioactive pollutants has become a priority in current research.

26

27 Various adsorbents, including carbon nanotubes, activated carbon, graphene oxide,
28 mesoporous silica, mesoporous carbon, clays, zeolites, metal-organic frameworks (MOFs), and
29 materials derived from agricultural or industrial wastes, have been developed for this purpose
30 [34]. Among these, synthesized zeolites have attracted particular attention due to their diverse
31 structures and chemical stability. Zeolites are microporous, aluminosilicate minerals that have
32 important properties useful for a variety of industrial and environmental applications. They
33 exist both in natural and artificial forms, and while they share many properties, there are also

1 distinct differences. Natural zeolites are formed through volcanic processes and are found in
2 large deposits. They have varying chemical compositions, typically containing sodium,
3 potassium, or calcium, and their structures can contain impurities, leading to slight
4 inconsistencies in pore size and ion exchange capacity. Artificial zeolites, on the other hand,
5 are synthetically engineered under controlled conditions, offering higher purity and more
6 uniform pore structures. This allows for precise control over properties such as cation exchange
7 capacity, thermal stability, and chemical resistance, making them highly effective in specific
8 industrial applications like catalysis, gas separation, and molecular sieving. While natural
9 zeolites are abundant and cost-effective, synthetic versions are tailored for specialized uses
10 requiring consistent performance. Analcime ($\text{NaAlSi}_2\text{O}_6 \cdot \text{H}_2\text{O}$) is indeed a fascinating type of
11 zeolite due to its unique structure and properties. Its ion exchange capability, resulting from its
12 three-dimensional framework of interconnected SiO_4 and AlO_4 tetrahedra, is highly effective
13 for adsorbing radioactive contaminants, making it suitable for environmental remediation.
14 However, obtaining pure natural analcime in sufficient quantities is rare and expensive [35,
15 36]. This has led researchers to explore cost-effective synthetic methods, such as the
16 hydrothermal method [37, 38], which allows for the production of analcime using inexpensive
17 raw materials like coal fly ash (FA), rice husk, or recycled glass (RG) [39-43]. These materials
18 provide a sustainable approach to producing zeolites, which are crucial for heavy metals,
19 radioactive contaminants adsorption, and other industrial applications. The conversion of
20 recycled glass and fly ash into synthetic zeolites via hydrothermal processes or into other
21 functional materials are particularly promising. They not only provide an opportunity to recycle
22 solid waste materials, but also addresses environmental concerns.

23 As far as environmental pollution is concerned, global solid waste generation has been
24 steadily increasing, with estimates exceeding 2.01 billion metric tons per year [44]. This
25 includes municipal, industrial, and hazardous waste, with significant contributions from
26 construction and demolition activities, which account for about 33% not managed in an
27 environmentally safe manner [44]. These mean that, they are either burned openly, dumped in
28 unregulated landfills, or disposed of in ways that pose risks to the environment and public
29 health. Among, recycled glass (RG) and fly ash (FA) are two major byproducts in this waste
30 stream. In fact, RG occupied 4–8% of the total annual wastes volume [1, 19, 45], whereas FA
31 is an offshoot mostly linked to coal combustion from electricity generating plants and is
32 categorized under industrial waste, with estimated annual volume of over 750 million tons [44,
33 46]. Indeed, urgent and effective strategies are needed to reduce the harmful impacts of

1 improper disposal of these two wastes. Implementing sustainable practices such as recycling
2 and reusing, alongside responsible disposal methods of these wastes, can greatly minimize
3 pollution risks. In this context, RG and FA have been repurposed in different applications such
4 as zeolites nanocomposites materials, construction materials, and alternatives to cement. For
5 instance, composites and synthesized zeolites adsorbents have been developed by employing
6 recycled glass containers [30, 43], fly ash [39], SnO₂ nanoparticles [47], graphene-based
7 materials [48], natural clinoptilolite [49], and Alginate/Bentonite nanocomposite [50] for
8 efficient treatment of wastewater pollutants. The possibility of using RG in the preparation of
9 zeolites is mainly related to the physicochemical properties and stability of the main chemical
10 composition of glass, e.g., silicate (SiO₂) and alumina (Al₂O₃). These two compounds are very
11 similar to zeolite in composition, thus, creating the likelihood of a synthesis of functional
12 minerals through a suitable hydrothermal reaction for its application as an adsorbent. These
13 properties also make it a versatile composites for the removal of harmful constituents [51],
14 such as pollutants treatment from wastewater, oils and organic [52], pathogenic bacteria [53],
15 and odors [54, 55]. Despite the extensive research on various forms of zeolites for adsorption
16 processes, none have specifically addressed the potential of glass-based zeolites for the
17 adsorption and treatment of radionuclides in marine environments. This gap in the literature
18 has inspired our research, driving us to explore the unique properties and potential advantages
19 of glass-based zeolites as a promising solution for mitigating radioactive contamination in
20 marine ecosystems. However, this objective cannot be fully achieved with the zeolite we have
21 synthesized from solid recycled glass, due to the nanoparticle size of the adsorbent, which
22 limits its practical application. Compounding this challenge is the consideration of large-scale
23 deployment in the dynamic marine environment, where strong water currents would impact the
24 efficiency of the zeolite. To address these issues, we developed the idea of compositing the
25 zeolite with permeable concrete, a material known for its porous structure and filtering
26 properties.

27 Permeable concrete (PC) is a specialized form of concrete identified by its inextricable
28 links of voids, which grant it a high degree of water permeability, distinguishing it from
29 conventional concrete. This environmentally friendly material is valued for its ability to support
30 sustainable infrastructure, offering benefits such as water purification, permeable pavements,
31 acoustic absorption, and thermal insulation. Its porous structure allows rainwater to pass
32 through, reducing surface runoff and promoting groundwater recharge, making it ideal for civil
33 engineering and construction applications. The interconnected pores in permeable concrete

1 usually range in diameter from 2 to 8 mm, with a void fraction of 15% to 35%. Its compressive
2 strength typically ranges from 2.8 to 28 MPa, offering both functionality and versatility. [56].
3 Permeable concrete generally comprises binder materials, coarse aggregates, water, and
4 admixtures. Ordinary Portland Cement (OPC) is commonly used as the binder in traditional
5 permeable concrete fabrication. However, in recent years, researchers have explored the usage
6 of fly ash as a binder material to produce high-performance porous or permeable concrete [57-
7 62]. Compared to OPC, the resulting geopolymer permeable concrete exhibits excellent
8 mechanical properties and improved durability, particularly in terms of chemical resistance to
9 acids and sulfates [63, 64]. The process of geopolymerization in the preparation of PC involves
10 using FA as the primary raw material, which is activated through an alkaline solution typically
11 composed of sodium silicate (Na_2SiO_3) and sodium hydroxide (NaOH). In this process, the FA
12 reacts with the alkaline activators, forming a three-dimensional aluminosilicate network that
13 provides the binding properties essential for concrete production. NaOH acts as a catalyst,
14 dissolving the silica and alumina present in FA, while Na_2SiO_3 aids in the polymerization
15 process, leading to the formation of a rigid and durable geopolymer matrix. This matrix binds
16 the coarse aggregates without the need for OPC, thus contributing to the environmental benefits
17 of reduced carbon emissions. As a result, using geopolymer binders for manufacturing
18 permeable concrete is a promising alternative, supporting both performance and sustainability.
19 Numerous studies have focused on enhancing pollutant removal efficiency in permeable or
20 pervious concretes [65-70]. However, research on the application of permeable concrete in
21 marine environments are limited, with most studies concentrating on the fabrication of artificial
22 reefs for marine pastures and coastal wetland berms [71-73]. Thus, using geopolymer-based
23 permeable concrete offers promising potential for ocean water cleaning applications.

24 In light of these challenges, this paper explores the synthesis and characterization of a
25 nano-engineered silica waste concrete composite specifically designed for the remediation of
26 Sr^{2+} and Cs^+ radionuclide contaminants. The developed radionuclide removal zeolite (RrZ) was
27 characterized using Scanning Electron Microscopy (SEM), Transmission Electron Microscopy
28 (TEM), and Brunauer–Emmett–Teller (BET) analysis to assess its structural and
29 morphological properties. The adsorption capability of both RrZ and the composite RrZ-fly
30 ash geopolymer (RrZ-FAGP) was evaluated through Inductively Coupled Plasma Mass
31 Spectrometry (ICP-MS). Additionally, X-Ray Diffraction with PDF crystalline phase analysis
32 and Fourier-Transform Infrared spectroscopy (FTIR) were conducted to further elucidate the
33 adsorption mechanisms. Finally, the adsorption performance of the developed porous

1 geopolymer concrete composite (PGCC) was thoroughly examined, focusing on critical
2 parameters such as adsorption efficiency, water permeability, and porosity. To optimize the
3 composite properties, Taguchi, variance, and Technique for Order of Preference by Similarity
4 to Ideal Solution (TOPSIS) analyses were employed, providing a comprehensive evaluation on
5 the efficacy of PGCC in radionuclide treatment.

6 **2. Experimental section**

7 **2.1 Materials**

8 Solid recycled glass (RG), fly ash (FA), and different fractions of natural gravel aggregate
9 (GA) are the primary solid raw materials used in this study. The waste glass bottles were
10 collected from Longgang District Recycling Plant (Shenzhen), and was only used in the
11 preparation of Radionuclide Removal Zeolite (RrZ). The recycled glass was washed, dried,
12 crushed to finer grit pieces, and grounded using a disc ball mill with 180 rpm speed for 30 min.
13 The obtained fine glass powder was then screened and particle size inferior to 5 μm was
14 collected. The FA and GA have been purchased from renowned suppliers. The FA is composed
15 of fine spherical particles of different sizes, whereas, three types of natural gravel aggregates
16 with different fractions of 3-6 mm, 6-9 mm and 9-12 mm were used in the preparation of the
17 porous concrete. A mixture of NaOH and Na_2SiO_3 is used to quicken the experiment. NaOH
18 in flake form was diluted into distilled water to prepare 6 M concentrated solution. The Na_2SiO_3
19 used is liquid water glass with 2.31 modulus and 42% baume degree. All of these materials are
20 used in the preparation of the porous geopolymer composite concrete (PGCC).

21 **2.2 Analytical techniques**

22 The chemical composition of the RG, FA, and the derived mesoporous zeolite powder were
23 tested by XRF, Thermo Fisher ARL Perform'X and the results are presented in [Table 1](#). The
24 results indicate that RG primarily comprises SiO_2 , Na_2O and CaO , with composition in wt %
25 equal to 69.43, 15.35, and 9.27% respectively, classified as silica glass. The chemical
26 composition of FA, in the other hand are SiO_2 , Al_2O_3 , Fe_2O_3 and CaO with different oxides
27 and elements values. The sum of the predominant oxides ($\text{SiO}_2 + \text{Al}_2\text{O}_3 + \text{Fe}_2\text{O}_3$) = 91.21% >
28 70%, thus the present FA mineral is categorized as Class F, according to ASTM C 618 standard
29 [\[74\]](#). In addition, it can also be seen that, Si and Al are the primary elements of FA, in which
30 the Si/Al molar ratio is equal to 1.16, confirming the suitability of the present FA in the
31 readiness of cementitious materials. The preselection of aggregates in the preparation of porous
32

1 concrete is of paramount importance. In this study, three size ranges of natural gravel aggregate
 2 were employed, 3-6 mm, 6-9 mm, and 9-12 mm, as mentioned early. Their respective apparent
 3 and bulk densities were calculated according to the Chinese standard JGJ52-2006 [75]. Fig. 1
 4 presents the raw materials used in the study, and Table 2 displays the aggregate densities
 5 corresponding to the different gradations.

6

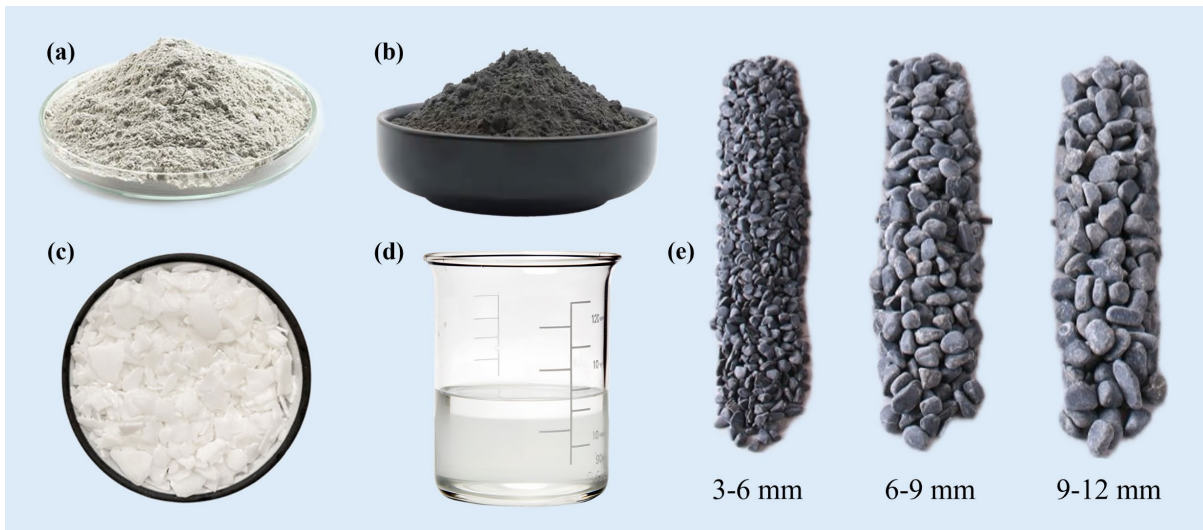
7 Besides, the chemical composition test, several experiments were performed to collect
 8 different details of the material. For instance, the concentrations variation of Sr^{2+} and Cs^+ from
 9 the contaminated solutions was evaluated by using ICP-MS, Thermo Scientific iCAP RQ. The
 10 surface morphology of the samples was analyzed by SEM, Microanalysis Oxford Instruments,
 11 Zeiss Gemini 300 X-MAXN. The TEM imaging, elemental distribution and oxides atomic
 12 fraction were collected on TEM, serried Talos F200X S/TEM. The BET surface area and the
 13 pore size distribution were measured by Micromeritics ASAP 2460. XRD crystalline patterns
 14 were obtained with XRD, D8 Advance, and the chemical bonds and functional groups of the
 15 material were identified by FTIR, Bruker invenio S.

16

Table 1 Recycled glass and fly ash chemical composition

Chemical oxides [Wt (%)]	SiO ₂	Al ₂ O ₃	CaO	Fe ₂ O ₃	MgO	TiO ₂	SO ₃	K ₂ O	Na ₂ O
Recycled Glass (RG)	69.43	2.03	9.27	0.47	1.69	0.07	0.13	0.68	15.35
Fly Ash (FA)	49.14	38.71	3.53	3.36	1.10	1.08	1.02	0.84	0.40

17



18

19 Fig. 1 Raw materials: (a) Recycled glass powder (RGP) having 69.43% SiO₂, 15.35% Na₂O and 9.27% CaO, (b)
 20 Fly ash (FA), (c) NaOH in flake form, (d) Na₂SiO₃ solution, (e) natural gravel aggregate (GA) with different
 21 fractions of 3-6 mm, 6-9 mm and 9-12 mm

22

Table 2 Aggregate gradation with their corresponding densities

Aggregate gradation	Apparent density (kg/m ³)	Bulk density (kg/m ³)
3-6 mm	2727.314011	1729.10
6-9 mm	2804.382739	1694.25
9-12 mm	2638.850044	1670.30

2.3 Synthesis and formation of the Radionuclide removal Zeolite (RrZ)

The radionuclide removal zeolite (RrZ) was prepared by a simple and clean hydrothermal process using recycled glass powder mixed into NaOH solution, following the research work of Dassekpo et al. [30]. The ratio of glass powder-to-NaOH solution (GP:NaOH) equivalent to 2:15 was adopted. The synthesized liquid was composed of 3 M NaOH solution, which was added into the measured glass powder, and mixed for about 5 min. The mixed slurry was then poured into a hydrothermal synthesis reactor, and imperviously sealed for 3 hours at a conditioning temperature of 150°C. After the conditioning and normal cooling, the resultant mixture was filtered through vacuum filtration equipment and thereafter continuously cleaned with deionized water to neutralize. Afterwards, the resultant solid product was subjected to an 80°C drying heat for 24 hours. Finally, the obtained zeolite crystals were grounded in agate mortar and pestle to make a uniform. The refined powder was stored in a suitable container to protect it from moisture and contaminants. Fig. 2 illustrates the synthesis process of the RrZ.

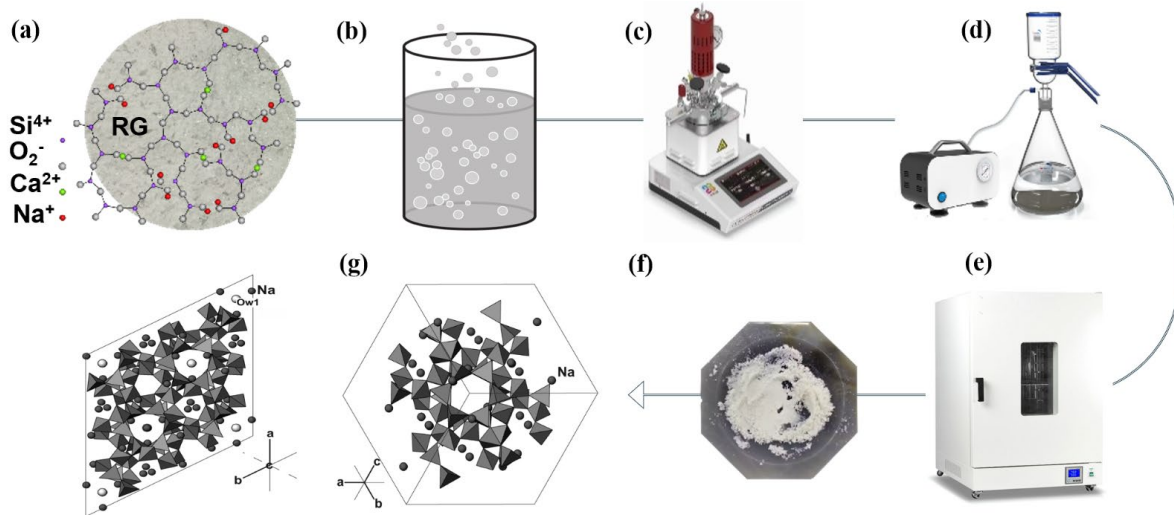


Fig. 2 Synthesis process of the radionuclide removal zeolite: (a) Recycled glass (RG), (b) Mixing of RG into NaOH solution, (c) Hydrothermal conditioning of the slurry, (d) Filtration and de-ionization, (e) Heating at 80°C for 24 h, (f) Grinding of the RrZ crystals, (g) Crystal structures of the radionuclide removal zeolite

3. Adsorption modeling and sampling process

3.1 Simulation of Sr²⁺ and Cs⁺

The simulated nuclide solutions were prepared by placing 0.1 g of RrZ powder into a beaker and adding 10 mL of a simulated radioactive solution containing Sr²⁺ and Cs⁺, each at adsorption of 10 mg/L. The simulated radioactive solutions were composed of strontium chloride (SrCl₂) and cesium chloride (CsCl), both of which are readily soluble in water. To achieve the desired concentrations, 0.018 g of strontium chloride and 0.0127 g of cesium chloride were precisely weighed using an analytical balance. These were then dissolved in distilled water acidified with nitric acid to prepare 1000 mL of solution, resulting in 10 mg/L of Sr²⁺ and Cs⁺ in separate batches. The suspension was stirred at room temperature of 25°C, mixing speed of 300 r/min, with the pH calibrated between 4-8.

3.2 Dissolution kinetics analysis on RrZ and RrZ-FA composite

In order to study the performance of the RrZ and FA composite, a preliminary laboratory test was undertaken to verify the adsorption capability of the composite RrZ-FA under the simulated Sr²⁺ and Cs⁺ contaminants. The mixtures were composed of the synthesized radionuclide removal zeolite (RrZ) and the principal fly ash (FA) raw material. For the composite, RrZ powder with different ratios of 5%, 10%, and 20% was mixed in different batches containing 95, 90, and 80% FA. For control, the adsorption mechanism of a mixture composed of only FA was also performed. The mixtures were labeled 5RrZ-FA, 10RrZ-FA, 20RrZ-FA and FA, respectively. Details of the mixtures proportion are presented in [Table 3](#). The solid powders (RrZ and FA, or FA) were first dry-mixed homogeneously in Hobart mixer for 3 min. After, the alkali activator composed of 6 Mol/L NaOH and Na₂SiO₃ with SiO₂/Na₂O ratio (modulus) of 1 was added in the mixture. The liquid-to-solid ratio (L/S) was pre-experimentally determined and was found to be equal to 0.33 to ensure optimal workability. The alkali activator was added in different mixtures and the slurry was mixed for about 5 min. Afterwards, the fresh slurry was poured in small silicon molds and exposed at ambient temperature for 7 days curing.

After the curing time, each sample of the mixtures was crushed and ground and the mass of 0.1g of the composite powder was collected. The powder was then mixed in 10 mL of a simulated radioactive solution containing Sr²⁺ and Cs⁺. The simulation method for Sr²⁺ and Cs⁺ solutions is described in [section 3.1](#). The suspension on each sample was stirred at a speed of 300 rpm/min in ambient temperature. Afterwards, a volume of 0.1 mL of each solution was taken at specific time intervals of 10, 30, 60, and 180 min by collecting the clear upper liquid

1 from the beaker. A 0.22 μm filtration membrane and a syringe filter were used to separate solid
 2 particles from the liquid. Each solution was then diluted 20-fold to obtain 2 mL of clean liquid.
 3 The clean liquid was suggested to a centrifuge for 5 min at 4500 rpm. It is important to
 4 emphasize that, for radionuclide removal zeolite (RrZ) dissolution analysis, only the RrZ
 5 powder was directly mixed in the simulated Sr^{2+} and Cs^{+} radioactive solution. The mass of the
 6 powder, the volume of the solution used, including the methodology, are the same as described
 7 above. Following centrifugation, the supernatant of each sample was filtered, and the molarity
 8 of Sr^{2+} and Cs^{+} in the filtered mixture were examined using ICP-MS. The ion concentrations
 9 in the supernatant were measured. The adsorption rate Q (%) and the adsorption capacity q
 10 (mg/g) of each sample were calculated using the following equations:

$$11 \quad Q = \frac{C_0 - C}{C_0} \times 100\% \quad (1)$$

$$12 \quad q = \frac{(C_0 - C)V}{m} \quad (2)$$

13 Where: C_0 is the initial concentration of ions in the solution (mg/L); C , the concentration
 14 of ions in the filtrate after adsorption (mg/L); m , the mass of adsorbent (g); and V , the volume
 15 of the solution (mL).

16 **Table 3** Mixtures proportion of RrZ-FA Composite

Mix	Solid materials (g)		Alkali activator (g)	
Label	RrZ powder	FA powder	NaOH	Na_2SiO_3
5RrZ-FA	6.25	118.75	36.19	33.97
10RrZ-FA	12.5	112.5	36.19	33.97
20RrZ-FA	25	100	36.19	33.97
FA	-	125	36.19	33.97

23 3.3 Optimal Mix Ratio Determination

24 To achieve optimal adsorption efficiency, the mix ratio for the porous geopolymer
 25 composite concrete (PGCC) was developed using Taguchi's method, based on a 3-factor, 3-
 26 level design. Pre-experimentation results determined that the paste-to-aggregate ratio (B/A)
 27 should be controlled between 0.15 and 0.2. To ensure water permeability, the target porosity
 28 (TP) was set between 15% and 25%. For the geopolymer slurry, a solution of NaOH and
 29 Na_2SiO_3 concentrations were used as the alkali activator, with a 6 M NaOH solution to promote
 30 early strength and facilitate curing at room temperature. The $\text{SiO}_2/\text{Na}_2\text{O}$ ratio for the activator

was set at 1. The liquid-to-solid ratio (L/S) was experimentally determined to be 0.33 for optimal workability. The mix ratio design followed a volumetric method, where the amount of each component was determined by the target porosity. Material dosages were calculated based on the void ratio of coarse aggregate, the water-to-fly ash ratio, sand content, and the target porosity, using eq. (3). Details of the mix ratio for the preparation of PGCC and the formulation of the simulated solutions are presented in Table 4.

$$\frac{m_g}{\rho_g} + \frac{m_e}{\rho_c} + \frac{m_f}{\rho_f} + \frac{m_w}{\rho_w} + \frac{m_s}{\rho_s} + \frac{m_a}{\rho_a} + v = 1 \quad (3)$$

Where, m_g , m_e , m_f , m_w , m_s , and m_a are the amount of coarse aggregate, cement, mineral admixture, water, fine aggregate, and admixture per unit volume of concrete (kg/m^3), respectively; ρ_g , ρ_c , ρ_f , ρ_w , ρ_s , and ρ_a are the apparent densities of coarse aggregate, cement, mineral admixture, water, fine aggregate, and admixture (kg/m^3), respectively; and v , the target porosity (%).

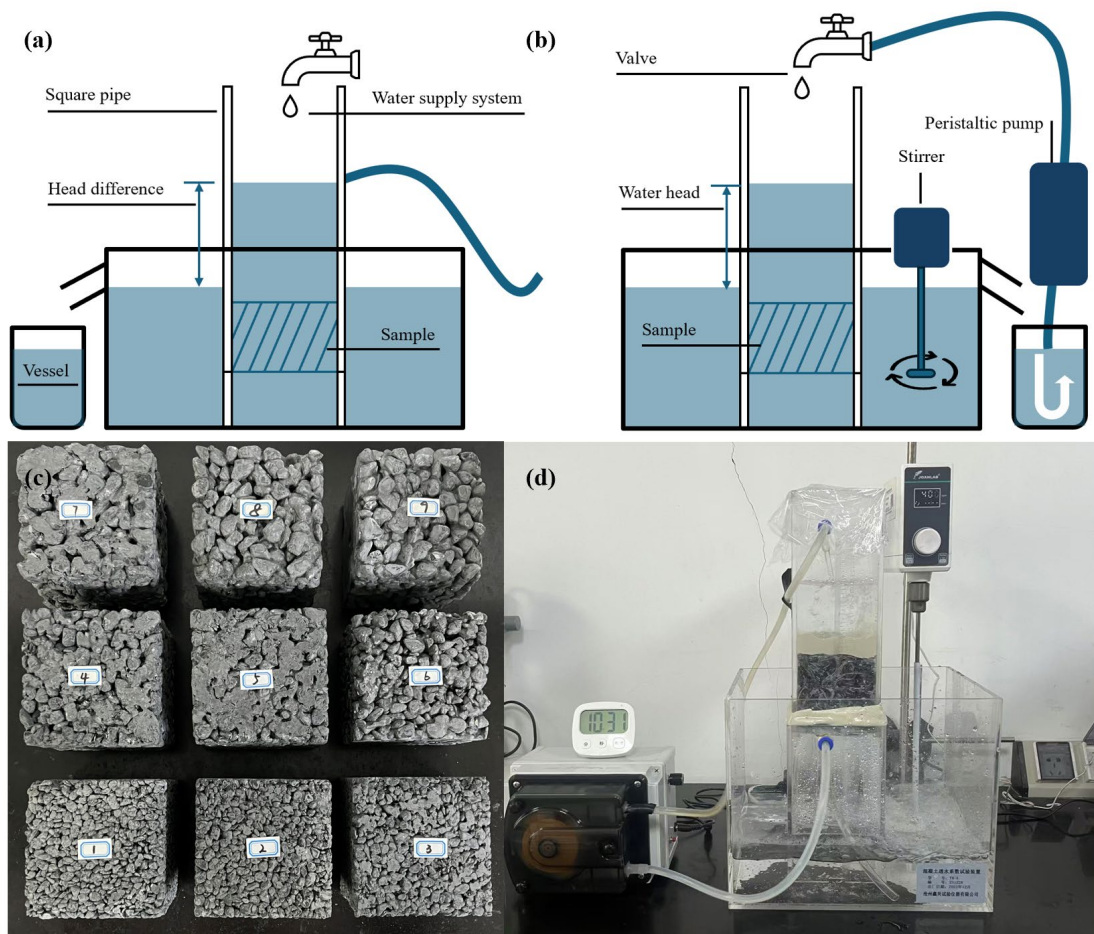
Table 4 Mix ratio for the preparation of PGCC (kg/m^3) and formulation of the simulated solutions (g)

Label	GA size	B/A	TP	GA	FA	RrZ	NaOH	Na ₂ SiO ₃	SrCl ₂ (g)	CsCl (g)
1	3-6 mm	0.150	25%	1700.6	130.7	32.7	47.3	44.4	0.295663826	0.165600341
2	3-6 mm	0.175	20%	1764.4	158.2	39.6	57.2	53.7	0.357881269	0.200448128
3	3-6 mm	0.200	15%	1824.8	187.0	46.8	67.7	63.5	0.423009032	0.236925975
4	6-9 mm	0.150	20%	1856.4	142.7	35.7	51.6	48.5	0.322749042	0.180770682
5	6-9 mm	0.175	15%	1917.3	172.0	43.0	62.2	58.4	0.388891546	0.217816882
6	6-9 mm	0.200	25%	1645.8	168.7	42.2	61.0	57.3	0.381496051	0.213674690
7	9-12 mm	0.150	15%	1875.1	144.1	36.0	52.1	48.9	0.325999450	0.182591225
8	9-12 mm	0.175	25%	1610.5	144.4	36.1	52.2	49.0	0.326657950	0.182960049
9	9-12 mm	0.175	20%	1673.3	171.5	42.9	62.0	58.2	0.387890151	0.217256004

3.4 Sampling Process

The sampling process for PGCC followed a strict methodology. The NaOH solution was prepared in advance and left for 24 h to ensure ionization equilibrium. The alkali activator consisted of this NaOH solution mixed with Na₂SiO₃ liquid, as mentioned previously, and the mixture was stirred for approximately 30 min before use. For the solid raw materials, FA and RrZ were mixed sequentially to form a homogeneous reactive powder. During preparation, the coarse aggregates were first combined with the activators, added gradually, and mixed thoroughly for about 3 min. Next, the dry pre-mixed reactive powder was incorporated into the wet aggregate slurry, and the heterogeneous mixture was stirred for 3 min to ensure the slurry has fully coated the aggregate surfaces. The remaining alkali solution was then added and

1 mixed for an additional 10 min. The fresh porous concrete samples were poured into 100 mm
 2 cubic molds in multiple layers, with each layer vibrated. The pressure from the compression
 3 testing machine on the final compacted samples was recorded. Finally, the samples were sealed
 4 with cling film and stored at an ambient temperature of 24°C and relative humidity RH=50%,
 5 until the final testing (Fig. 3c). It is important to emphasize that, to simulate the adsorption
 6 performance to reflect the real marine environment, an ion adsorption cycling device was
 7 designed and fabricated for the circumstance. The device was customized, and, in some cases,
 8 accessories were linked to it during the experiment to satisfy each stage of the experiment. The
 9 different illustrative parts of the device and the casted porous geopolymer concrete composite
 10 (PGCC) with different aggregate gradations are illustrated in Fig. 3(a, b, and d).



11
 12 **Fig. 3** (a) Constant head water permeability test system, (b) Ion adsorption cycling system, (c) Prepared PGCC
 13 with different aggregate gradation, (d) Customized permeability and adsorption cycling system

14
 15 The permeability test and adsorption cycling test were carried out by filling the storage
 16 tank with 5.0 L of the prepared simulation solution. A mass of 1 mg Sr and Cs solution
 17 corresponding to 1 g of adsorbent composed of geopolymers mixed with RrZ, was formulated
 18 according to the slurry in the coordination ratio. These 9 types of solution were determined

1 based on the binder in 9 different proportions of PGCC. The dosage of the simulated SrCl_2 and
2 CsCl powders for the different samples corresponding to 5.0 L adsorbent was calculated, and
3 the results are presented in [Table 4](#). Before filling, the valve of the system was closed, and later
4 turned to 45° when the first filtrate was collected in the tank. When the solution in the upper
5 part of the storage tank reached the specified height, the power supply of the pump was turned
6 on, putting the whole device in a self-circulating state. Afterwards, two test tubes of the filtrated
7 solution were collected from the outlet at the initial passage at different time frames of 10, 30,
8 60, 120 min. The tubes were hermetically sealed and stored in a secure cabin. After stabilization
9 of the water flow, a volume of the liquid was taken from the front and rear water sources for
10 testing. The solution was taken and filtered through a $0.22\ \mu\text{m}$ syringe cartridge and was further
11 diluted to 20-fold with distilled water to obtain 2 ml clear liquid. The resulting solution was
12 tested by ICP-MS, and the dissolution degree of Sr^{2+} and Cs^+ in the samples was recorded.

13

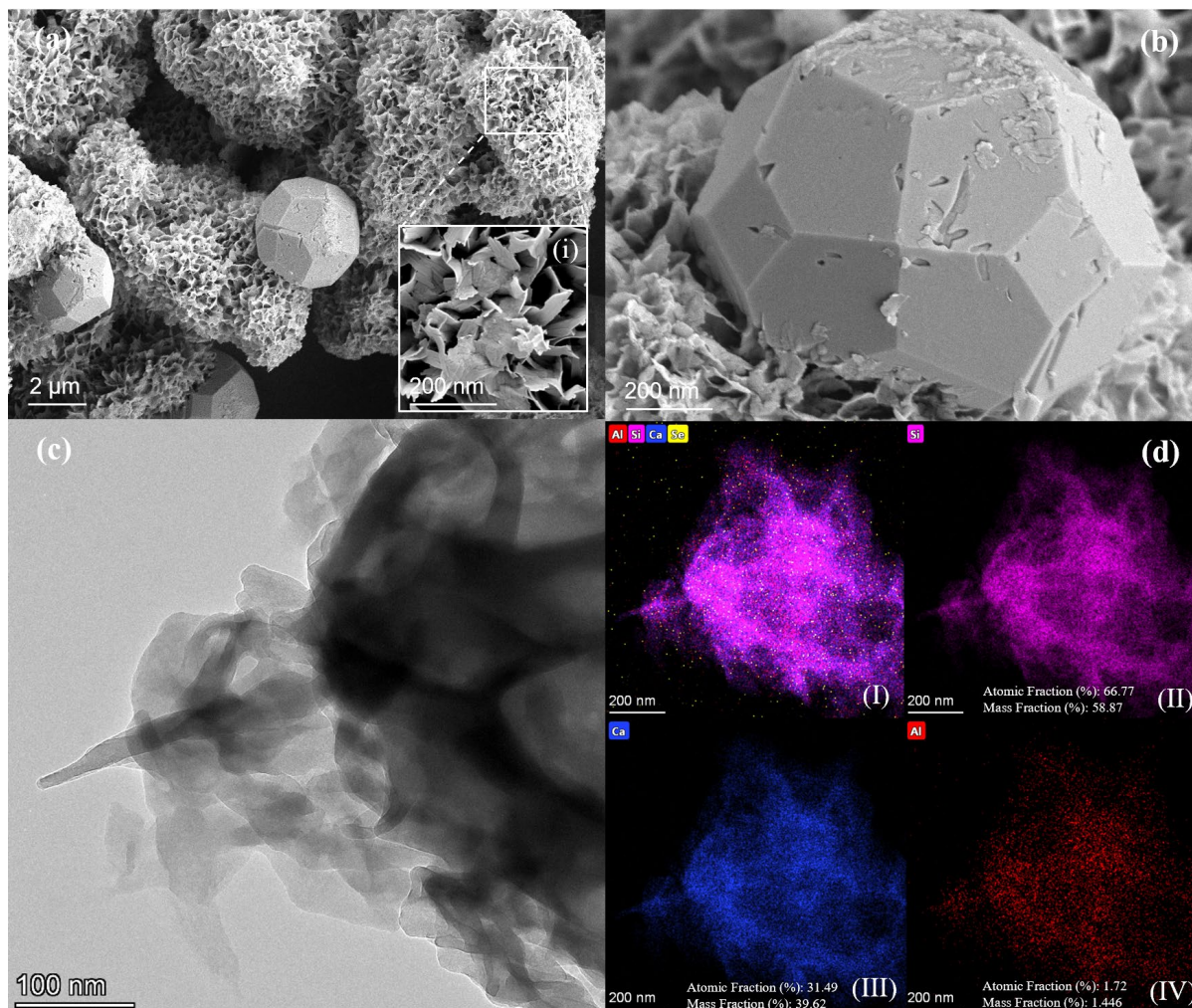
14 **4. Results and Discussions**

15 **4.1 Characterization of the Radionuclide Removal Zeolite (RrZ)**

16 After the hydrothermal synthesis, the developed radionuclide removal zeolite powder
17 morphology was characterized by SEM, TEM, and BET, and the findings are presented in [Fig.](#)
18 [4](#). It is observable from the SEM micrograph, a structure composed of thin lamellas
19 agglomerated and distributed over the entire surface, and the formation of two large single
20 crystals ([Fig. 4a](#)). The micrograph of the lamellas portion collected at 200 nm magnitude shows
21 clearly the open aspect of the structure ([Fig. 4b](#)). In general, the zeolite nucleation is often
22 affected by different factors such as the supersaturation degree of nucleation revulsion and the
23 reaction solution. The large-scale single crystals observed in the structure can be explained by
24 a moderate degree of nucleation, as it was demonstrated that, until the crystals grow to the
25 largest sizes, the small amount of nucleation can effectively supply enough reactive species in
26 the reaction system [[76](#), [77](#)]. The permeability of the structure can be attested to the fact that
27 the glass micro spheres become soft and soluble during the hydrothermal reaction in NaOH
28 dissolution. At this stage of decomposition, the particles lose weight, and the pressure induces
29 vaporized gas, which generates pores in the structure of the formed crystals.

30 The microscopic appearance and distribution of RrZ nanoparticles was also checked by
31 the aid of TEM ([Fig. 4 c-h](#)). In general, the thinness of the fibers that make up RrZ zeolite can
32 be observed. The black specks below the fiber surface ([Fig. 4 c](#)) are the result of the aggregation
33 and deposition of RrZ nanoparticles at a later stage of synthesis. The distinctive chemical

1 elements are also evenly distributed on the surface (Fig. 4 d). Si and Ca are high-density
 2 elements with atomic fractions of about 66.77% and 31.49%, respectively (Fig. 4 e, f). The
 3 tiniest traces of Al and Se are also visible at 1.72% and 0.02%, respectively (Fig. 4 g, h). From
 4 the TEM results, it can be understood that the derived RrZ is characterized by the discrete
 5 nanoparticles with homogeneous pore surface, which results in the eminent adsorption property.



6
 7 **Fig 4.** Characterization of the synthesized RrZ adsorbent: (a) SEM micrograph showing agglomerated structure
 8 and formation of large single crystals, (i) High magnitude of the structure with the appearance of thin and large
 9 lamellas pores, (b) SEM large-scale of the single crystals observed in the structure, (c) TEM fiber showing black
 10 specks at the surface, (d) TEM mapping of RrZ adsorbent showing: (I) Combined elements distribution, (II) Si
 11 oxide distribution mapping, (III) Ca oxide distribution mapping, and (IV) Al oxide distribution mapping.

12
 13 In addition, the BET surface area and the pore size distribution of the RrZ powder were
 14 measured by Micromeritics ASAP 2460. The surface area was recorded to be around 63.69 m²
 15 g⁻¹, with Langmuir surface area of about 70.24 m² g⁻¹, and desorption hysteresis P/P₀ between
 16 = 0.7 to 1.0. Between 1.0-300 nm, the cumulative surface area is around 52.61 m² g⁻¹ and 55.76
 17 m² g⁻¹, respectively for BJH adsorption and desorption; while at 1.7-300 nm, the DH revolves
 18 around 42.91 m² g⁻¹ and 47.18 m² g⁻¹, respectively, for adsorption and desorption cumulative

1 surface area. Furthermore, the average diameter of desorption and adsorption pores were,
 2 respectively, 22.04 and 15.74 nm, indicating the high porosity of the synthesized zeolite, and
 3 its allegiance to type IV isotherm class for adsorbents based on IUPAC (International Union
 4 of Pure and Applied Chemistry) guidelines. This is a proof that the prepared RrZ adsorbent has
 5 mesopores, which align with the characteristics of the adsorption and desorption pores
 6 diameters of 22.04 and 15.74 nm discussed earlier, because mesopores are known as pores with
 7 diameters between 2 nm and 50 nm. In terms of dispersion, RrZ is characterized by analcime,
 8 a feldspar-like mineral classified as a zeolite. Analcime belongs to the cubic crystal system
 9 (Ia3d) and typically forms regular tetrahedral-trisectahedral crystal shapes, with unit cell
 10 parameters of $a = 1.370$ nm. Its framework consists primarily of four-membered, six-
 11 membered, and eight-membered rings, with the six-membered rings forming the main channels
 12 [78]. These channels have a one-dimensional, non-intersecting structure with a diameter of
 13 approximately 0.26 nm. Consequently, analcime's structure is relatively dense, with a porosity
 14 of only 0.18. In addition to its common cubic symmetry, $\text{NaAlSi}_2\text{O}_6 \cdot \text{H}_2\text{O}$ can also exist in other
 15 symmetry types, such as triclinic, monoclinic, and orthorhombic, depending on the conditions
 16 of its formation, with temperature being the primary influencing factor [79].

17

18 4.2 Adsorption Capability of RrZ and RrZ-FA Composite

19 To further investigate the adsorption process of pure RrZ and the composite RrZ-FA,
 20 adsorption tests were conducted on both materials. Three kinetic models were employed,
 21 namely quasi-first-order, quasi-second-order, and intra-particle diffusion. These models are
 22 employed to illustrate the adsorption rate as a function of contact time. It showed that, the
 23 adsorption kinetics of the adsorbent are mainly explored by two kinetic models, namely the
 24 quasi-primary kinetic model [80] and the quasi-secondary kinetic model [81], and from a
 25 mechanistic point of view by using Boyd's model [82]. The mathematical formulation of these
 26 models is described as follows:

$$27 \quad \ln(q_e - q_t) = \ln q_e - \frac{k_1}{2.303} t \quad (7)$$

$$28 \quad \frac{t}{q_t} = \frac{1}{k_2 q_e^2} \cdot \frac{t}{q_e} \quad (8)$$

$$29 \quad B_t = -0.4977 - \ln(1 - F) \quad (9)$$

30 Where t designates the adsorption time (min), q_t and q_e denote, respectively, the adsorption
 31 at time t , and the adsorbed amount per unit mass (mg/g) when equilibrium is reached. The
 32 quasi-primary kinetic rate constant (min^{-1}) is expressed through k_1 and the quasi-secondary

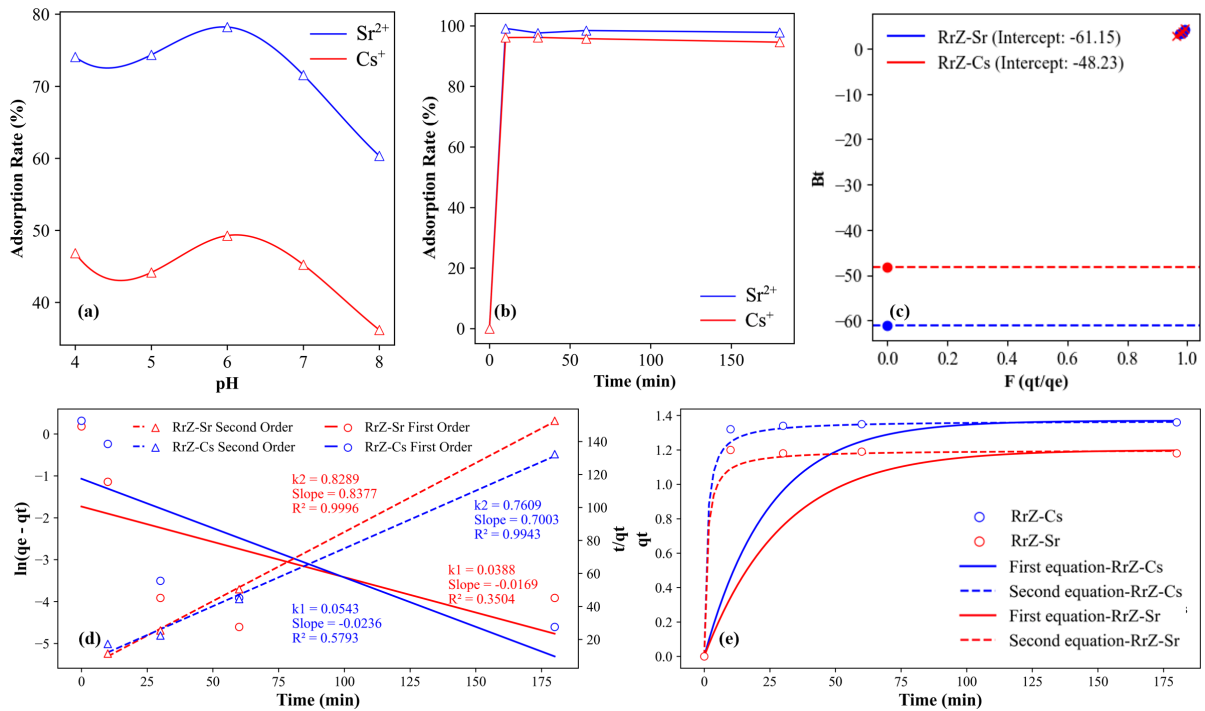
1 kinetic rate constant [g/(mg min)] is expressed through k_2 . Plotting t with the help of $\lg(q_e - q_t)$
2 yields k_2 , and plotting t with the help of t/q_t yields k_2 and q_e [83].

3 During the adsorption process, the solution's pH and equilibrium duration are critical
4 factors. The pH influences the adsorbent by altering its surface charge and degree of
5 protonation, as well as affecting the molarity of model ions in the mixture [84, 85]. Equilibrium
6 duration is particularly significant from an economic perspective when treating contaminants.
7 Therefore, the optimal pH and equilibrium duration for RrZ were first investigated. The pH
8 evaluation results indicate that a pH of 6 is favorable for the negatively charged RrZ adsorbent,
9 and thus, a pH value of 6 was adopted for further kinetic studies (Fig. 5a). The adsorption
10 efficiency of Sr and Cs ions by RrZ was also analyzed as a function of time. The dissolution
11 test followed the procedure outlined in section 3.2, where ICP-MS was employed to record the
12 concentrations of Sr^{2+} and Cs^+ after exposure to pure RrZ. The adsorption efficiency for both
13 ions was calculated and is presented in Fig. 5(b). The results show a sharp increase in
14 adsorption during the initial stage (approximately within the first 30 min), followed by a
15 gradual deceleration as equilibrium was reached. The adsorption efficiency of RrZ on Sr^{2+} and
16 Cs^+ solutions with a concentration of 10 mg/L reached up to 99.16% and 96.14% within 10
17 min, respectively, achieving equilibrium in the later stages.

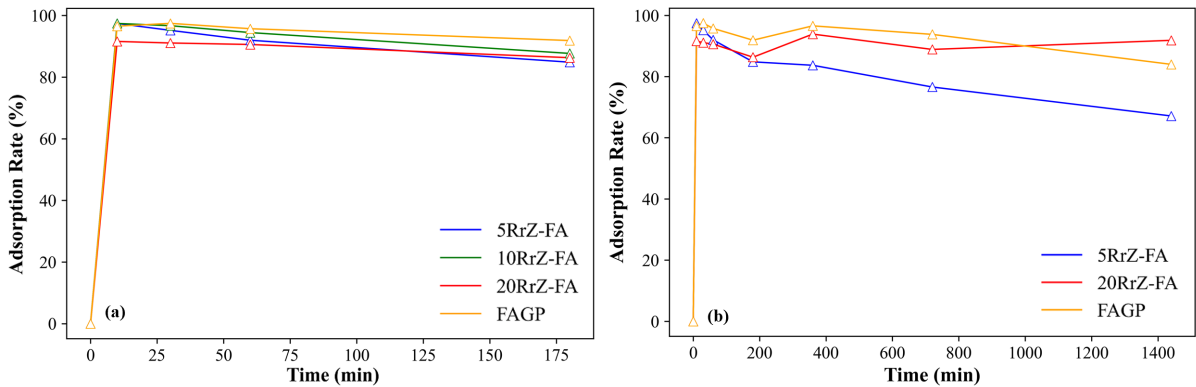
18 To further understand the kinetics, Boyd's model, based on Eq. (9), was employed. If the
19 graph of Bt against time (t) is a straight line with zero intercept, the process is driven by intra-
20 particle diffusion. If the plot shows an intercept, whether linear or nonlinear, the process is
21 dominated by film diffusion. In this study, the adsorption of Sr^{2+} and Cs^+ by RrZ is controlled
22 by film diffusion, as indicated in Fig. 5(c). These findings demonstrate that synthesized RrZ
23 exhibits high adsorption performance, making it suitable for treating radionuclide contaminants.

24 Additionally, regression analysis of the adsorption kinetics for Sr^{2+} and Cs^+ ions using
25 pure RrZ was performed based on Eqs. 7 and 8. The slopes were obtained, and the k_1 and k_2
26 values for RrZ and both ions (Sr^{2+} and Cs^+) were calculated to be approximately 0.0388, 0.8289,
27 0.0543, and 0.7609, respectively. From these results, the correlation coefficients for the quasi-
28 first-order and quasi-second-order kinetic models were derived for Sr^{2+} and Cs^+ . As illustrated
29 in Fig. 5(d), the R^2 value of 0.9996 from the fitting of the quasi-second-order kinetic equations
30 was superior to that of the quasi-first-order kinetic equations, showing that the adsorption of

1 Sr^{2+} and Cs^{+} by RrZ is consistent with the quasi-second-order kinetic model, with
 2 chemisorption playing a key role in the process.



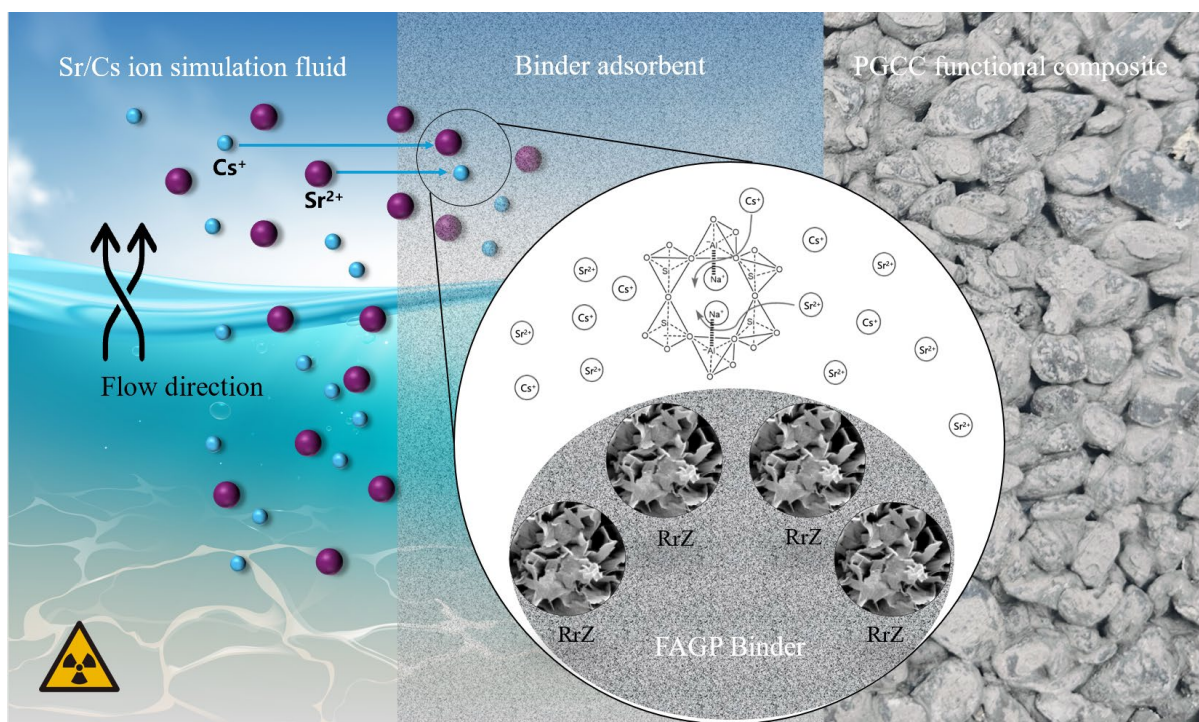
3
 4 **Fig. 5** Adsorption kinetics of RrZ on Sr^{2+} and Cs^{+} ions: (a) Effect of pH, (b) Effect of contact time, (c) Intra-
 5 particle diffusion Boyd model, (d) Quasi-first-order and quasi-second-order models, (e) Kinetic modeling of Sr^{2+}
 6 and Cs^{+} ion adsorption



7
 8 **Fig. 6** Adsorption efficiency of Sr^{2+} and Cs^{+} ions: (a) Adsorption behavior in 5, 10, 20% RrZ mixed in fly ash
 9 (FA) compared to fly ash geopolymer (FAGP) mixture, (b) Adsorption behavior in 5, 20% mixed in fly ash (FA)
 10 compared to fly ash geopolymer (FAGP) mixture

11 A comparative investigation of the RrZ and fly ash geopolymer (RrZ-FA) composite was
 12 conducted, focusing on its significance as the primary binder in the preparation of the porous
 13 concrete. The samples were prepared following the methodology detailed in [section 3.2](#), with
 14 the exception that coarse aggregates were omitted, and only the geopolymer paste matrix was
 15 used. After curing, the adsorption efficiency of the crushed sample powders for Sr^{2+} and Cs^{+}

1 was tested at intervals of 0, 30, 60, and 180 min. Fig. 6 presents the adsorption performance of
 2 RrZ-FA composites containing 5%, 10%, and 20% RrZ adsorbent, alongside a control using
 3 100% FA as the adsorbent. As shown in Fig. 6(a), both RrZ and FA demonstrated excellent
 4 adsorption performance, reaching up to 90% efficiency within 10 min. To further analyze the
 5 long-term behavior, the adsorption test was extended to 24 h using samples with 100% FA and
 6 5% or 20% RrZ (Fig. 6b). In the later stages, it was observed that FA did not maintain its
 7 adsorption efficiency, with desorption occurring, whereas the sample containing 20% RrZ
 8 mixed with FA exhibited stable and superior performance. Consequently, the mixture of 20%
 9 RrZ and 80% FA was selected as the optimal ratio for the preparation of PGCC. The schematic
 10 illustration of the adsorption of Sr^{2+} and Cs^+ by PGCC incorporating RrZ is presented in Fig.
 11 7.



12
 13 Fig. 7 Illustration of the adsorption of Sr^{2+} and Cs^+ by the porous geopolymer composite concrete (PGCC)
 14 incorporating Radionuclide removal Zeolite (RrZ)

16 4.3 XRD-PDF Crystalline Phase

17 To analyze the reaction products of the developed PGCC, the crystalline phases of various
 18 binding components were examined. In addition to phase analysis of the synthesized pure
 19 analcime adsorbent (RrZ) and the fly ash geopolymer (FAGP), tests were conducted on both
 20 RrZ and FAGP after their use in Sr^{2+} and Cs^+ adsorption. For this analysis, wet solid powders
 21 were collected from the Sr^{2+} and Cs^+ contaminated liquids at 10 min and 24 h, respectively.

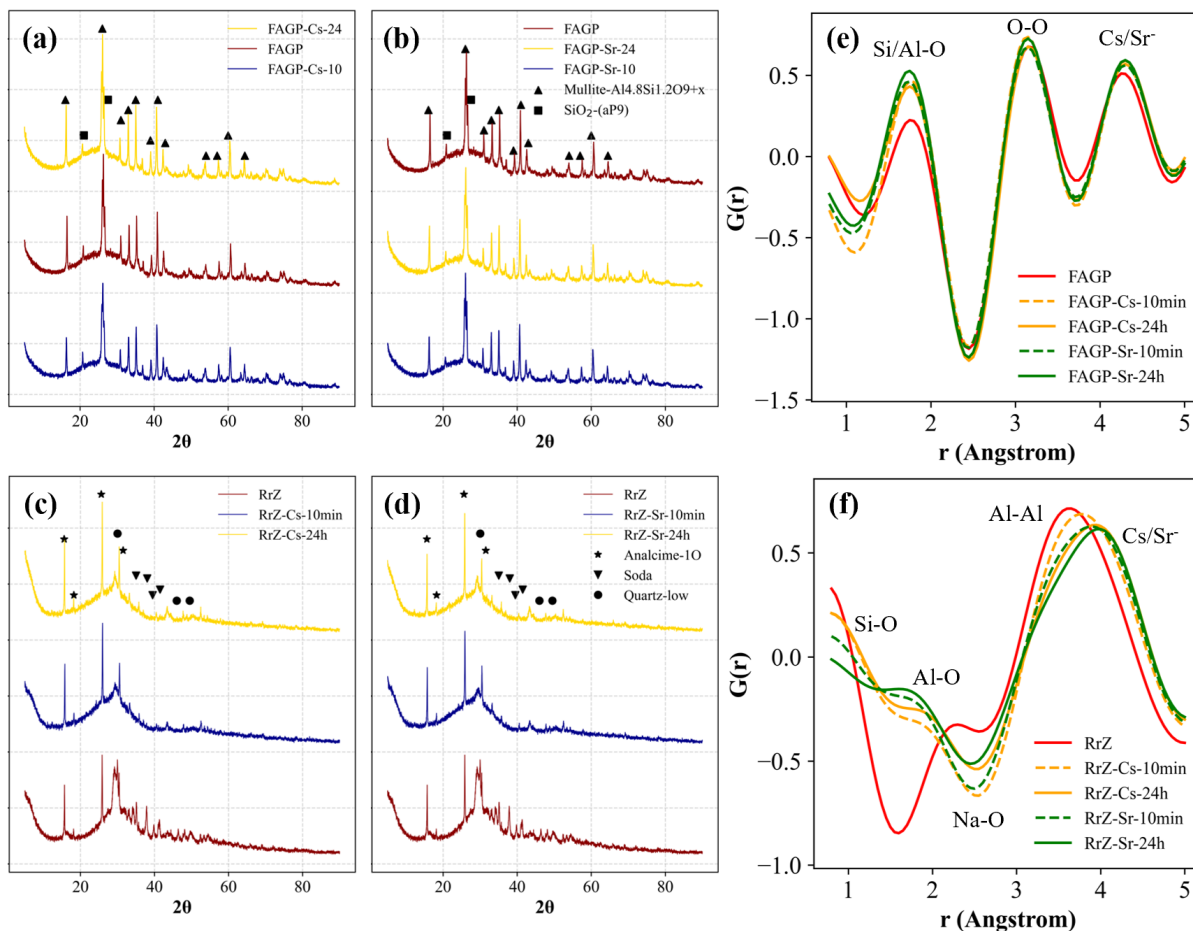
1 The mixtures were labeled as RrZ-Cs-10min, RrZ-Cs-24h, RrZ-Sr-10min, RrZ-Sr-24h; and
2 FAGP-Cs-10min, FAGP-Cs-24h, FAGP-Sr-10min, and FAGP-Sr-24h to correspond to both
3 Sr^{2+} and Cs^+ radioactive nuclides at different contact times. The samples were then subjected
4 to temperature control at 60°C for 24 h, after which the dried powders were collected for XRD
5 analysis. The XRD patterns describing the crystalline phase results of the samples are shown
6 in Fig. 8(a-d).

7 Three main crystalline phases, analcime ($\text{NaAlSi}_2\text{O}_6 \cdot \text{H}_2\text{O}$), sodium carbonate (Na_2CO_3),
8 and low-phase quartz (SiO_2) were observed in the RrZ samples (Fig. 8b). SiO_2 and Al_2O_3 were
9 the primary minerals in the hydrothermal treatment of silicate glass, which led to the conversion
10 of these glass minerals into pure analcime zeolite. The dominant diffraction peaks of analcime
11 suggest that hydrothermal conditioning was sufficient to produce pure analcime zeolite. The
12 other phases, such as sodium carbonate, likely formed during ambient storage of the analcime
13 powder as free Na^+ ions reacted with oxygen and carbon dioxide in the air. Additionally,
14 although a small amount of low-phase quartz remained after the reaction, it did not affect the
15 overall structure. Notably, no quartz or sodium carbonate phases were detected after the RrZ
16 was exposed to water during the adsorption process.

17 RrZ samples that underwent ion exchange adsorption with Sr^{2+} and Cs^+ exhibited
18 increased peak intensities for RrZ-Cs and RrZ-Sr compared to the original RrZ, even after 10
19 min and 24 h of contact (Fig. 8a, b). These changes in peak intensities, which increased over
20 time, are primarily due to shifts in atomic positions or changes in atomic density in the unit cell
21 [86]. Although Cs^+ has a larger ionic radius than Na^+ , it can still penetrate the zeolite's open
22 pores and remain within the structure. The 8R centers' spacing size is well-matched to Cs^+
23 ionic radius, which differs from the distribution of Na^+ ions [87]. The structural changes
24 observed in the zeolite after substituting Na^+ with Cs^+ or Sr^{2+} are primarily attributed to
25 differences in ionic radii, which may cause slight distortions in the zeolite A structure, as well
26 as variations in the interactions between the zeolite framework and the cations, impacting the
27 planar spacing [86].

28 In the mixture containing FAGP, mullite ($\text{Al}_{4.8}\text{Si}_{1.2}\text{O}_{9+x}$) and quartz (SiO_2 -aP9) were the
29 primary mineralogical phases (Fig. 8d). During polymerization in a NaOH solution, the peaks
30 of mullite and quartz were enhanced as part of the amorphous portion was consumed by crystal
31 growth or defect formation. The intensity of the crystal peaks decreased and shifted to lower

1 angles due to the addition of sodium silicate, which precipitates as amorphous silica and is
 2 consumed by mullite and quartz. Since Si-O bond lengths are shorter than Al-O bond lengths,
 3 the addition of more Si-O bonds to the crystal structure causes a peak shift according to Bragg's
 4 law. However, it is important to note that mullite and quartz are both dense aluminum silicates,
 5 which do not possess significant adsorption capacity for heavy metal cations [88]. Thus, the
 6 amorphous fraction is likely the component responsible for adsorption.



7
 8 **Fig. 8** XRD crystalline phases and pair distribution function (PDF) results: (a) FAGP-Cs-24, FAGP and FAGP-
 9 Cs-10 patterns, (b) FAGP, FAGP-Sr-24 and FAGP-Sr-10 patterns, (c) RrZ, RrZ-Cs-10min and RrZ-Cs-24h
 10 patterns, (d) RrZ, RrZ-Sr-10min and RrZ-Sr-24h patterns; (e) PDF of FAGP, FAGP-Cs-10min, FAGP-Cs-24h,
 11 FAGP-Sr-10min, and FAGP-Sr-24h, (f) PDF of RrZ, RrZ-Cs-10min, RrZ-Cs-24h, RrZ-Sr-10min, and RrZ-Sr-
 12 24h.

13 **Figs 8(c, d)** compare the XRD patterns of FAGP with samples subjected to ion exchange
 14 with different cations. No new steps were recorded in the ion exchange process, nor any
 15 significant diffraction peaks associated with Cs or Sr compounds detected. Both nuclides
 16 retained their original structures, indicating that only ion exchange occurred. Interestingly, after

1 ion exchange with the cations, indistinct condensation peaks appeared around 20-30°, possibly
2 due to structural deformation of the fly ash geopolymer, similar to that observed in zeolites
3 during geopolymerization [89]. The XRD spectra showed that peak intensities of FAGP-Cs
4 and FAGP-Sr decreased after 10 min of adsorption compared to the uncontaminated FAGP
5 sample. However, after 24 h, the peak intensities of FAGP-Cs and FAGP-Sr became higher
6 than the original FAGP, likely due to the later desorption of the cations, as mentioned
7 previously.

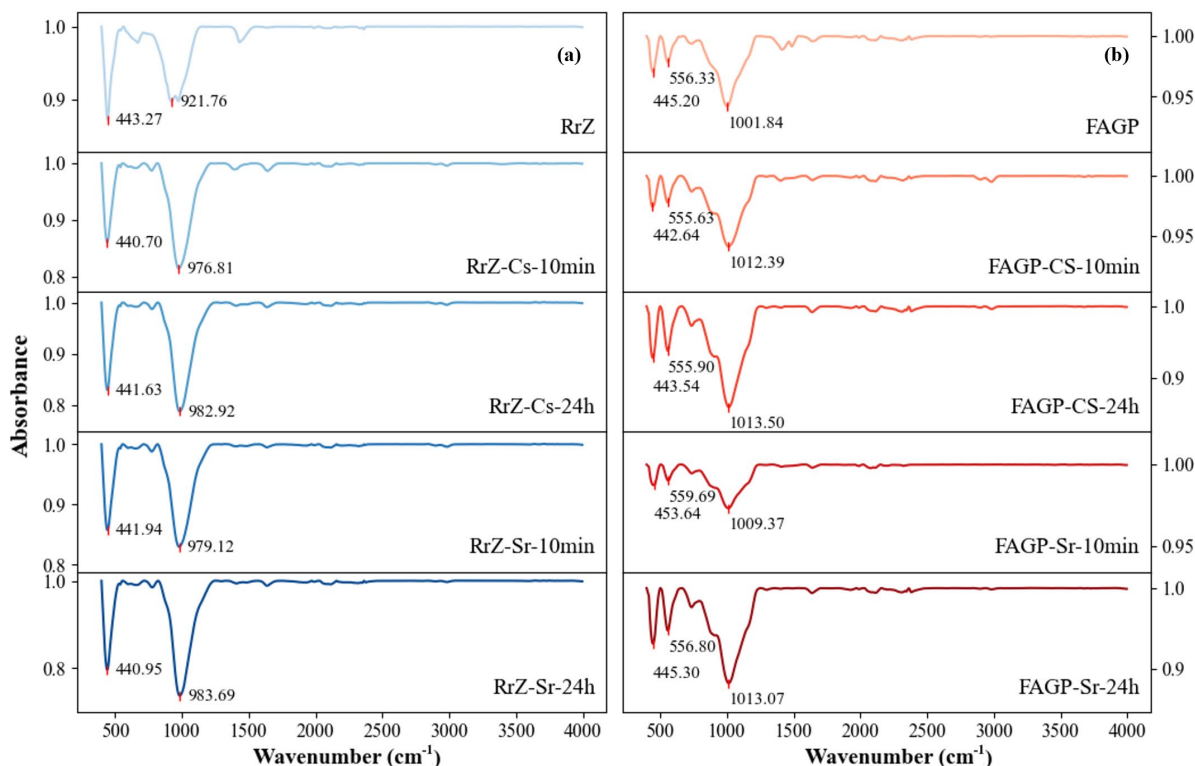
8 In addition, the atomic structure of RrZ and FAGP, both before and after adsorption, was
9 analyzed using PDF readings of the XRD diffractograms, as shown in Fig. 8 (e, f). The major
10 interatomic distances correspond to T-O, Na-O, O-O, T-T, and Na-T bonds, where T represents
11 Si or Al in tetrahedral sites. The first prominent peak, around 1.67 Å, arises from the
12 overlapping T-O bonds in the (Si, Al)O₄ tetrahedra. This is due to the similar bond lengths of
13 Si-O (1.61 Å) and Al-O (1.75 Å), which X-rays cannot easily distinguish. The height at
14 approximately 2.3 Å is broadly characterized to the Na-O distance in the eight-membered ring.
15 In this region, two peaks may appear at 2.1 Å and 2.4 Å, potentially corresponding to Na-O
16 vectors in different ring structures [90, 91]. The Na-O distance at 2.1 Å may be linked with a
17 four-membered or double-quaternary ring, while the 2.4 Å peak may correspond to a six-
18 membered or double-quaternary ring.

19 Typically, there are two types of T-T connections: Si-Si and Al-Si, with bond lengths of
20 approximately 3.1 Å and 3.3 Å, respectively. This small difference is mainly attributed to the
21 varying bond lengths of Si-O and Al-O. The peaks at 3.1 Å and 3.25 Å are interpreted as Si-Si
22 and Si-Al connections in adjacent tetrahedra [92]. Therefore, the Si-Al content at 3.25 Å is
23 expected to be greater than the Si-Si content at 3.1 Å, indicating that alternating Si-Al
24 connections predominate. Additionally, direct Si-Si connections may occur randomly within
25 the FAGP structure, aligning with the observed Si/Al ratio.

26 4.4 FTIR Adsorption Characterization

27 To further elucidate the adsorption mechanisms of RrZ and FAGP, FTIR analysis was
28 conducted to characterize their adsorption behavior (Fig. 9). The FTIR spectra of RrZ and
29 FAGP after 10 min and 24 h of Sr²⁺ and Cs⁺ adsorption results were also compared with the
30 spectra of the original samples. The post-adsorption spectra showed only minor changes
31 compared to the originals, indicating small shifts in band positions. These shifts suggest that

1 the chemical structures of RrZ and FAGP remain largely unchanged after ion exchange with
 2 Sr^{2+} or Cs^+ . Both materials exhibited similar peaks near 440 cm^{-1} and 1000 cm^{-1} bands,
 3 although FAGP showed an additional peak at 555 cm^{-1} . The band corresponding to the in-plane
 4 bending vibrational mode of water molecules appeared between 1620 and 1650 cm^{-1} across all
 5 samples, with no significant shifts observed due to changes in cations or adsorption time. The
 6 band from 1650 - 1850 cm^{-1} , representing the T-O-T (T = Si/Al) telescopic vibrational mode
 7 [93], showed a decrease in peak intensity over time following ion exchange with Sr^{2+} or Cs^+ .

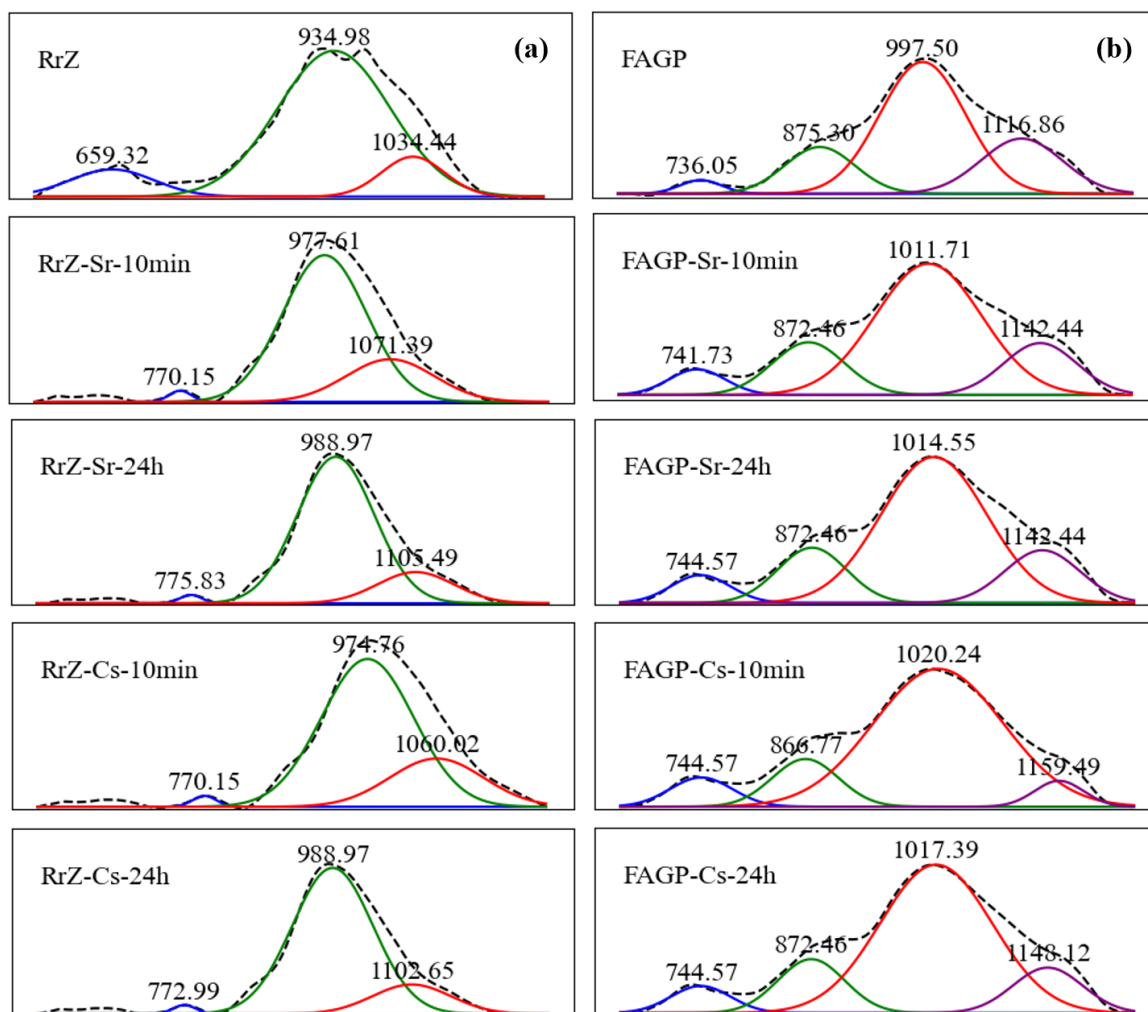


8
 9 **Fig. 9** FTIR absorption spectra of Sr^{2+} and Cs^+ after adsorption: (a) By RrZ, RrZ-Cs-10min, RrZ-Cs-24h, RrZ-Sr-
 10 10min, and RrZ-Sr-24h, (b) By FAGP, FAGP-Cs-10min, FAGP-Cs-24h, FAGP-Sr-10min, and FAGP-Sr-24h

11 The sharp band at 443.27 cm^{-1} is attributed to the T-O bending mode, which may result
 12 from the interaction of Sr^{2+} extra charge with either Al-O or Si-O bonds. This may also account
 13 for the slight shift of the band toward 440 - 441 cm^{-1} in the RrZ spectrum. Since Cs^+ has the
 14 same charge as Na^+ , it does not carry an additional charge and thus cannot interact strongly
 15 with the zeolite framework. However, the larger ionic radius of Cs^+ may tighten the zeolite
 16 framework, leading to an increase in wave numbers for bands representing either Al-O or Si-
 17 O bonds [94]. Another prominent band at 556.33 cm^{-1} corresponds to the symmetric stretching
 18 vibration of the bending variation and connecting bond of the T-O-T bond [95]. The peak shifts
 19 recorded after cation exchange suggest that cations with larger radii exert a greater influence

1 on the geopolymer structure. This effect may be due to the stronger attraction between larger
 2 cations, like Sr^{2+} and Cs^+ , and the oxygen atoms in the structure, which can lead to longer T-O
 3 bond lengths and corresponding shifts in their stretching vibrations [96].

4 Additionally, peak fitting of the frequency band between 1200 and 650 cm^{-1} revealed
 5 several isolated peaks, as shown in Fig. 10. The high-frequency band is due to the T-O-T (T =
 6 Si/Al) antisymmetric vibrations of the TO_4 unit [97]. The peaks near 997.5 cm^{-1} and 934.98 cm^{-1}
 7 cm^{-1} are likely due to asymmetric T-O-T vibrational modes, indicating the presence of AlO_4
 8 units. In contrast, the band around 880 cm^{-1} corresponds to the Si-OH bending mode. When
 9 Sr^{2+} and Cs^+ replace Na^+ , the adsorbate molecules diffuse through an 8R open pore with a
 10 diameter of approximately 0.4 nm [98]. As a result, only molecules with radii smaller than 0.2
 11 nm can access the inner cavity of the zeolite. The ionic radii of Sr^{2+} and Cs^+ , the target ions
 12 being exchanged for Na^+ (0.095 nm), are 0.169 nm and 0.113 nm , respectively. [95]. During
 13 the reaction of RrZ with Sr^{2+} and Cs^+ containing solutions, some of the Na^+ ions in the zeolite
 14 structure are replaced by Sr^{2+} and Cs^+ .



15 Fig. 10 FTIR absorption spectrum split peak fitting: (a) For RrZ, RrZ-Cs-10min, RrZ-Cs-24h, RrZ-Sr-10min, and
 16 RrZ-Sr-24h, (b) For FAGP, FAGP-Cs-10min, FAGP-Cs-24h, FAGP-Sr-10min, and FAGP-Sr-24h
 17

4.5 Adsorption performance of the developed PGCC

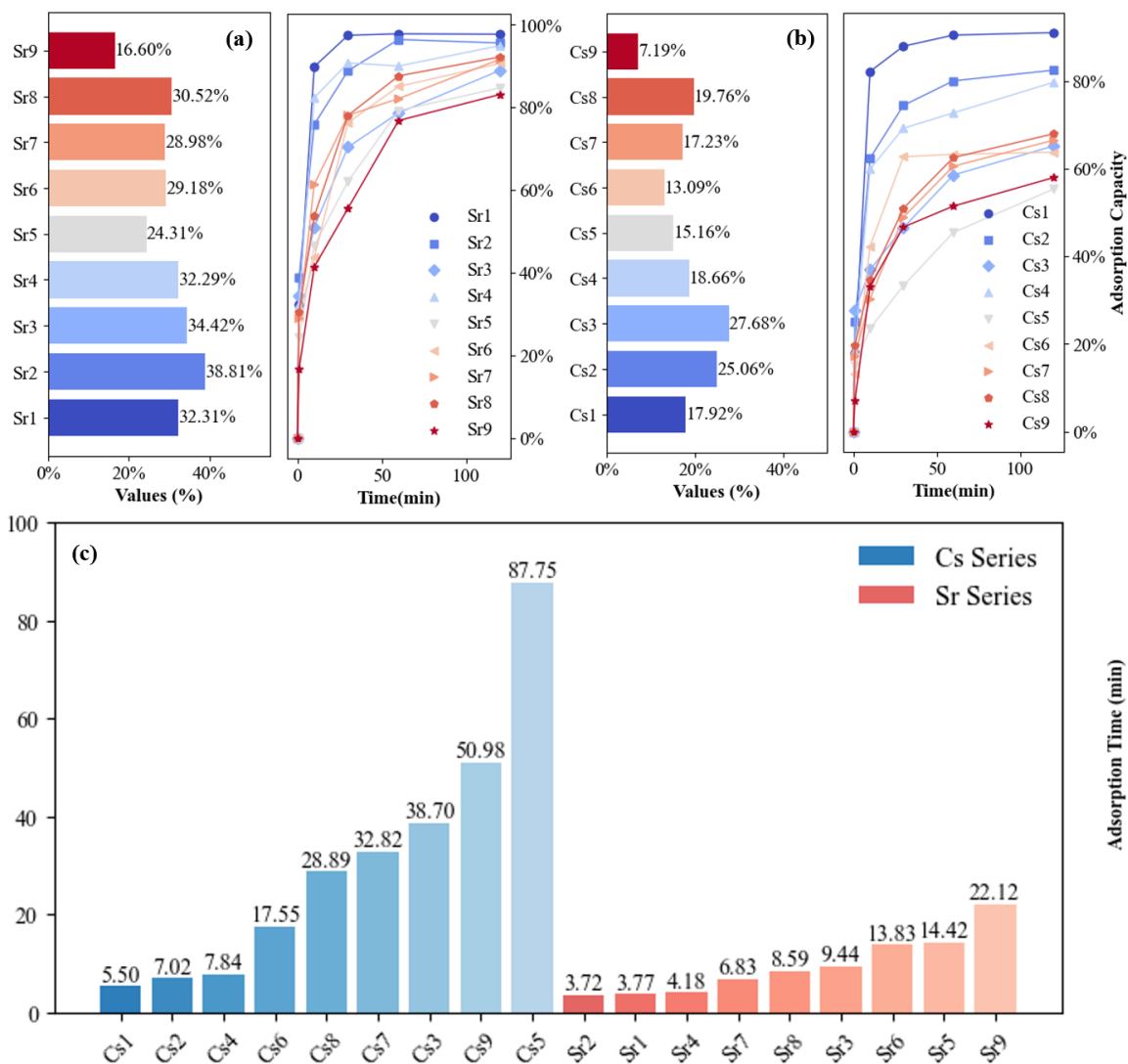
This section analyzes and discusses the adsorption performance of the developed porous geopolymer concrete composite (PGCC), covering aspects such as adsorption efficiency, water permeability, porosity, as well as Taguchi, variance, and TOPSIS analyses.

4.5.1 Adsorption efficiency analysis

The single-cycle adsorption trends of Sr and Cs ions over time for the 9 samples groups are shown in Fig. 11, with the final removal rates provided in Table 5. It is important to emphasize that the single-cycle refers to the amount of 5.0 L of simulated liquid that passes through the PGCC in one cycle. Overall, the concentration of Sr and Cs ions in the simulated nuclide solutions decreased across all groups, though to varying degrees. For Sr ions, the single-cycle adsorption rate ranged from 16.6% to 38.81%, while Cs adsorption fell between 7.19% and 27.68%. In all tested samples, Sr exhibited higher adsorption efficiency compared to Cs. The highest single-cycle adsorption for Sr was observed in sample 2, while for Cs, sample 3 showed the optimal adsorption (Fig. 11a). These results reflect the immediate adsorption efficiency of PGCC in contact with Sr and Cs ions. As illustrated in Fig. 11(b), the adsorption rapidly increased during the early stage for all samples, reaching equilibrium within 120 min. The final adsorption degree for Sr remained higher than that of Cs, ranging from 83.13% to 97.71% for Sr and 55.31% to 91.01% for Cs. The specific adsorption rates are listed in Table 5. For Cs, the difference in final adsorption performance was smaller and more effective for Sr. However, the magnitude of the final adsorption rates did not exactly match the single-cycle trends. The differences can be attributed to the experimental conditions, including a fixed volume of water (5L) and varying constant flow rates, which influenced the adsorption dynamics in the later stages.

To provide a more comprehensive analysis of the adsorption velocity, the duration required for every sample to reach 50% adsorption was analyzed, with the results shown in Fig. 11(c). Darker colors indicate higher adsorption efficiency, achieved in a shorter time. In general, Sr adsorption efficiency was higher and more consistent across samples compared to Cs, where efficiency varied more and reached lower values at longer contact times, up to 87.75 min. The ranking of samples by adsorption efficiency also differed between Cs and Sr, with the exception of samples 1, 2, and 4, which remained relatively stable in both cases. In contrast, sample 7

1 showed significant variability, with considerable differences in the adsorption efficiency of Cs
 2 and Sr.



3
 4 Fig. 11 Adsorption capacity at 50% contact time: (a) For Sr samples, (b) For Cs samples, (c) Recapitulation of Sr
 5 and Cs series

6 Table 5 Final adsorption efficiency of Sr and Cs

Label	Final adsorption of Sr (%)	Final adsorption of Cs (%)
1	97.71	91.01
2	95.59	82.44
3	88.94	65.15
4	94.94	79.67
5	84.74	55.31
6	90.65	63.74
7	91.64	66.45
8	92.20	67.94
9	83.13	57.94

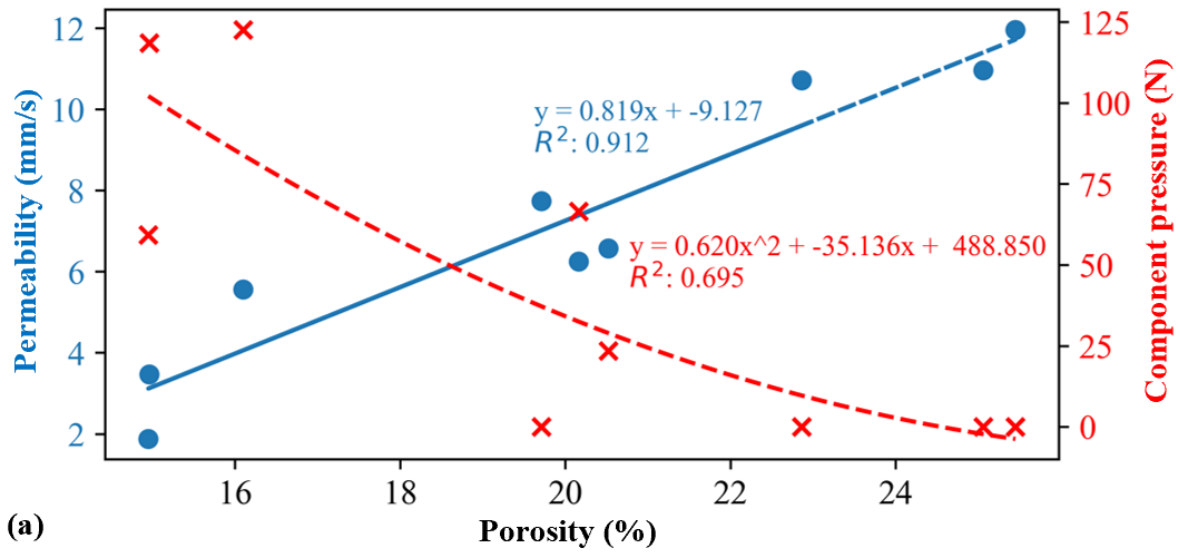
4.5.2 Porosity and water permeability analysis

The water permeability and porosity of PGCC were analyzed, and the findings are presented in Table 6. The porosity values of PGCC ranged from 25.45% to 14.95%, aligning well with the designed porosity. This is influenced by the preparation pressure, as the target porosity is determined by calculating the crown densities of the components, and it often exceeds the porosity at the natural packing density of the aggregates. Increasing the density of PGCC through applied pressure is essential to achieving the target porosity. Additionally, Table 6 shows that for a given aggregate size, the applied pressure during sample preparation tends to increase as porosity decreases, as illustrated in Fig. 12(a). However, the fit is imperfect due to the presence of zero values, indicating cases where the stack porosity is close to or below the target porosity, or influenced by varying aggregate sizes.

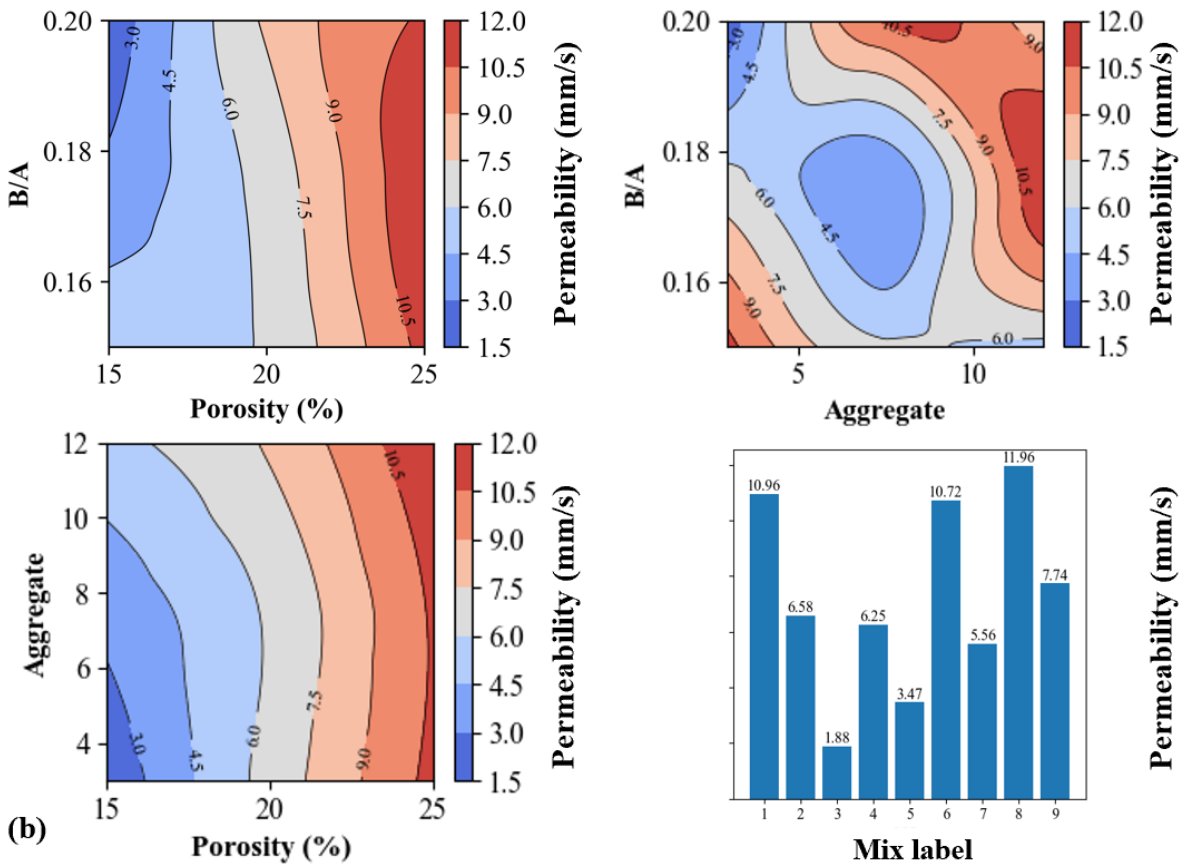
Table 6 also reveals that the permeability coefficients of the PGCC samples range from 1.876 to 11.956 mm/s. sample 3, with an aggregate size of 3–6 mm, B/A ratio of 0.2, and a target porosity of 15%, exhibits the lowest permeability coefficient, below 1.876 mm/s. In contrast, sample 8, with an aggregate size of 9–12 mm, a B/A ratio of 0.175, and a target porosity of 25%, has the highest permeability coefficient at 11.956 mm/s. Samples 1 and 6 also demonstrate high permeability coefficients of 10.962 and 10.716 mm/s, respectively. Notably, the target porosity for these three larger samples is 25%, yet their B/A ratios vary with aggregate size. These results suggest that permeability and B/A ratios do not consistently correlate with aggregate size; instead, porosity plays a more critical role. This conclusion is supported by the regression curve in Fig. 12(a), where a linear relationship between porosity and permeability coefficient is observed ($R^2 = 0.912$). This insight can be used to anticipate the permeability of PGCC based on porosity.

Table 6 Porosity, pressure and permeability results summary

Label	Aggregate	B/A	Target porosity (%)	Component pressure (MPa)	Porosity (%)	Permeability (mm/s)
1	3-6 mm	0.15	25	0	25.06	10.963
2	3-6 mm	0.175	20	0.0023495	20.52	6.576
3	3-6 mm	0.2	15	0.0059235	14.95	1.876
4	6-9 mm	0.15	20	0.0066561	20.16	6.247
5	6-9 mm	0.175	15	0.0118538	14.96	3.471
6	6-9 mm	0.2	25	0	22.86	10.716
7	9-12 mm	0.15	15	0.0122563	16.10	5.561
8	9-12 mm	0.175	25	0	25.45	11.956
9	9-12mm	0.2	20	0	19.71	7.739



(a)



(b)

1

2 Fig 12 Porosity and permeability analysis: (a) Permeability vs porosity analysis, (b) Porosity and aggregate in
3 regard to B/A, (c) Porosity vs Aggregate and NO analysis

4 The effect of PGCC design parameters on permeability was further examined using
5 bivariate contour plots (Fig. 12b). The plots show that permeability values exceeding 7.5 mm/s
6 are achieved when porosity surpasses 20%. In this scenario, variations in B/A and aggregate
7 size have minimal impact on permeability, as indicated by the low contribution in the ANOVA

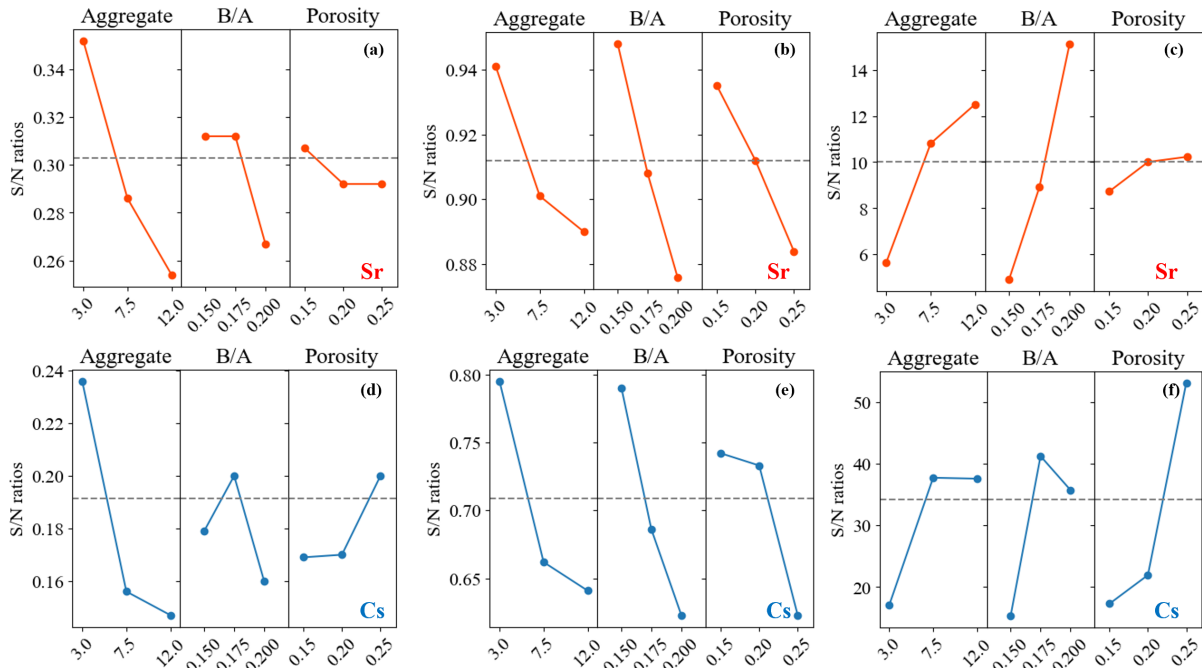
1 section. Larger aggregate sizes with lower B/A ratios lead to improved permeability when the
2 gap ratio is below 20%. From the contour plots of aggregate size versus B/A ratio, permeability
3 decreases when the aggregate size is in the range of 5–10 mm and the B/A ratio is between
4 0.16 and 0.18, with permeability dropping below 4.5 mm/s. However, increasing aggregate
5 size or the B/A ratio results in higher permeability. These findings indicate that focusing solely
6 on one design factor in PGCC may lead to suboptimal permeability performance.

7 The data were analyzed for average target/response functions, and Taguchi's method was
8 used to examine variations in response by applying selected signal-to-noise (S/N) ratios. The
9 S/N ratio represents the ratio of the mean (signal) to the standard deviation (noise). This study
10 focuses on the "larger is better" quality characteristic, as the goal is to maximize the strength
11 of the PGCC. Fig. 13 presents the average S/N values for all three control factors and highlights
12 the main effects of these parameters on the average response. The analysis revealed that
13 different aggregate particle sizes, B/A ratios, and porosity positively influence various
14 adsorption properties of PGCC. Adsorbent efficiency and maximum adsorption were
15 optimized with larger aggregate sizes, lower B/A ratios, and smaller porosity, which enhanced
16 adsorption performance. This is consistent with the previously described changes in
17 permeability coefficients.

18 Furthermore, the analysis showed a direct relationship between adsorbent efficiency,
19 maximum adsorption, and permeability coefficients. For higher permeability coefficients in
20 PGCC, the adsorbent has greater total water contact with the simulated solution over the same
21 time. Since adsorption efficiency and maximum adsorption volume maintain a linear
22 relationship within a certain adsorption range, faster flow rates may be critical for improving
23 adsorption efficiency. For single-cycle adsorption, the total water contact volume remained
24 consistent across all 9 samples, but the single-cycle completion time was negatively correlated
25 with the permeability coefficient. As a result, the optimal ratios for adsorption did not fully
26 align with those for permeability. Notably, smaller aggregate sizes still provided superior
27 adsorption performance, while the optimal B/A ratio and porosity varied depending on the
28 adsorbed ions. For example, Cs adsorption was favored by a B/A of 0.175 and higher porosity,
29 whereas Sr adsorption benefited from lower B/A ratios and porosity.

30 Using Taguchi's optimization process, the optimal mixing ratios for the three-performance
31 metrics, single-cycle adsorption rate, maximum adsorption capacity, and adsorption efficiency

1 were determined based on the signal-to-noise (S/N) ratio, focusing on one performance per
 2 every differentia. The maximum mixing ratios for the single-cycle adsorption rate for Cs and
 3 Sr ions adsorption were A1B2C3 and A1B2C1, respectively. For both maximum adsorption
 4 capacity and adsorption efficiency for Cs and Sr ions, the optimal ratios were A1B1C1. Due to
 5 the high correlation between maximum adsorption capacity and adsorption efficiency, the same
 6 optimal mix was identified for both: an aggregate size of 3–6 mm, a B/A ratio of 0.15, and a
 7 porosity of 25%. Thus, Taguchi's method demonstrates that achieving excellent combined
 8 adsorption properties in permeable PGCC requires a specific mix configuration.

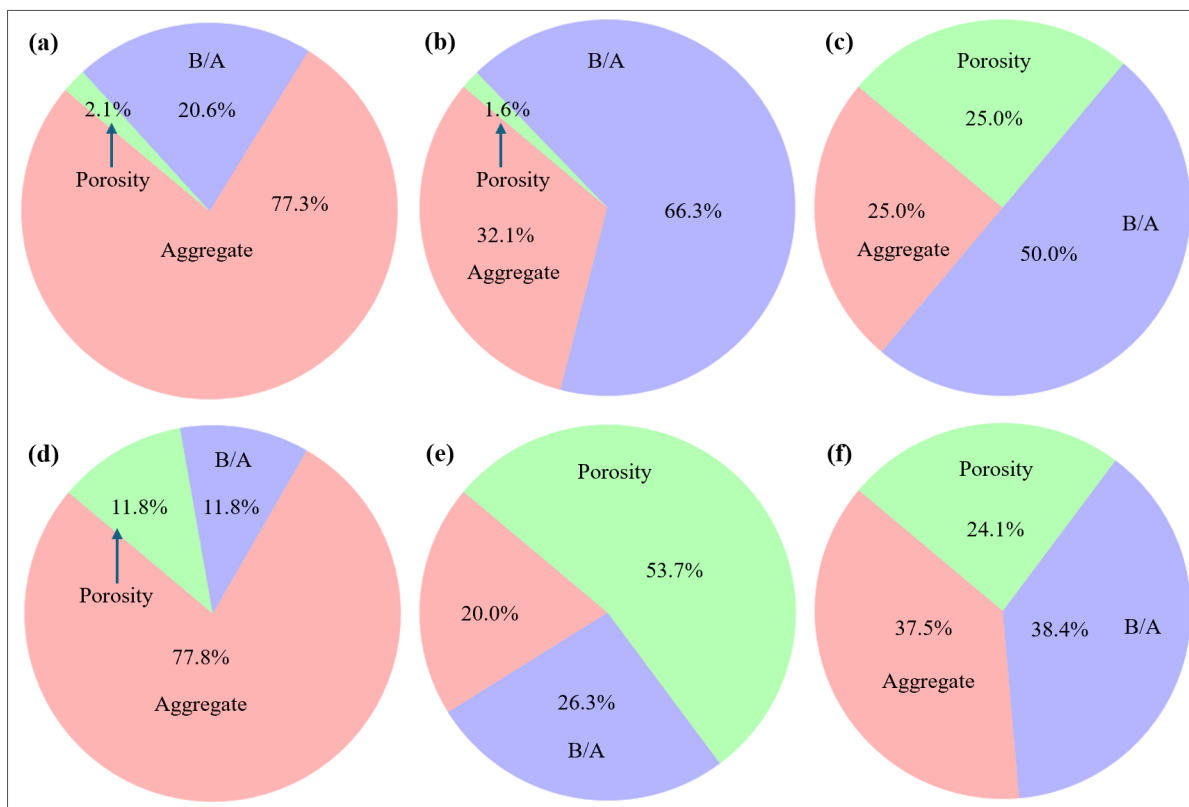


9
 10 **Fig. 13** Taguchi analysis using orthogonal array based Gaussian quadratic functions: (a) Single-cycle adsorption
 11 of Sr, (b) Maximum adsorption of Sr, (c) Adsorption efficiency of Sr; (e) Single-cycle adsorption of Cs, (f)
 12 Maximum adsorption of Cs, (g) Adsorption efficiency of Cs

13
 14 **4.5.3 Variance analysis**

15 The contribution of every element to the single-cycle adsorption rate, maximum adsorption
 16 rate, and adsorption efficiency was assessed using analysis of variance (ANOVA) at a 95%
 17 confidence level. To calculate each factor's contribution, the deviation sums of squares were
 18 summed to obtain the total deviation sum of squares (SST), and the percentage contribution of
 19 each factor was determined by calculating its proportion of the SST. As shown in Fig. 14,
 20 aggregate size had the highest contribution to single-cycle adsorption, accounting for
 21 approximately 77%, followed by porosity and the B/A ratio. For maximum adsorption, the
 22 contributions of the three factors for Cs were distributed roughly equally, whereas for Sr, the
 23 B/A ratio accounted for 50%, with the other two factors splitting the remaining contribution.

1 In terms of adsorption efficiency, the factor contributions varied more for Cs than for Sr.
 2 Specifically, porosity contributed 53.7% to Cs adsorption, while B/A contributed 66.3% to Sr
 3 adsorption. Furthermore, the comparison shows that Sr adsorption consistently exhibited
 4 higher contributions across all properties compared to Cs, underscoring the role of extra
 5 electrons in Sr structure and confirming that a higher B/A ratio provides a larger adsorption
 6 area. Cs, on the other hand, was more influenced by the porosity.



7
 8 **Fig. 14** Contribution of each factor using analysis of variance (ANOVA) at a 95% confidence level: (a) Single-
 9 cycle adsorption of Sr, (b) Maximum adsorption of Sr, (c) Adsorption efficiency of Sr; (e) Single-cycle adsorption
 10 of Cs, (f) Maximum adsorption of Cs, (g) Adsorption efficiency of Cs,

12 4.5.4 TOPSIS analysis

13 The Taguchi analysis method optimizes factor levels by calculating the signal-to-noise
 14 ratio for a single attribute or response. However, to optimize the ratio of multiple attributes
 15 simultaneously, the TOPSIS-based Taguchi method is employed. This approach evaluates the
 16 target response by measuring its distance from both ideal positive and negative solutions. The
 17 process begins by normalizing the original data matrix and using the cosine method to identify
 18 the best and worst solutions from the available options. The distances between each evaluation
 19 object and the optimal and worst solutions are then calculated, allowing for the determination
 20 of each object's relative proximity to the optimal solution, which serves as the basis for
 21 assessing its strengths and weaknesses.

1 A custom-weighted TOPSIS method was employed, with four different optimization
 2 schemes designed. The quality criteria were weighted using a full scale of 10 points.
 3 Normalized weights were derived based on the ratio of each differential's weight to the total
 4 weight of the attribute under consideration. Table 7 presents the normalized weights for each
 5 criterion, while Figs. 15 and 16 illustrate the proximity factors for Sr and Cs adsorption under
 6 the four optimization schemes. The first scheme aimed to optimize single-cycle adsorption
 7 performance by placing less emphasis on maximum adsorption capacity and adsorption
 8 efficiency. In contrast, the second and third schemes prioritized maximizing maximum
 9 adsorption capacity and adsorption efficiency, respectively, while reducing the focus on other
 10 performance metrics. The fourth scheme, the performance balance scheme, assigned equal
 11 weight to each criterion.

12

Table 7 Normalized weights for each criterion

Response Criterion	Target	S1	S2	S3	S4
Single cycle	Formula (12)	0.8	0.1	0.1	0.33
Maximum	Formula (12)	0.1	0.8	0.1	0.33
Efficiency	Formula (13)	0.1	0.1	0.8	0.33

13

Table 8 Approximation factors for Sr adsorption by the four-optimization scheme

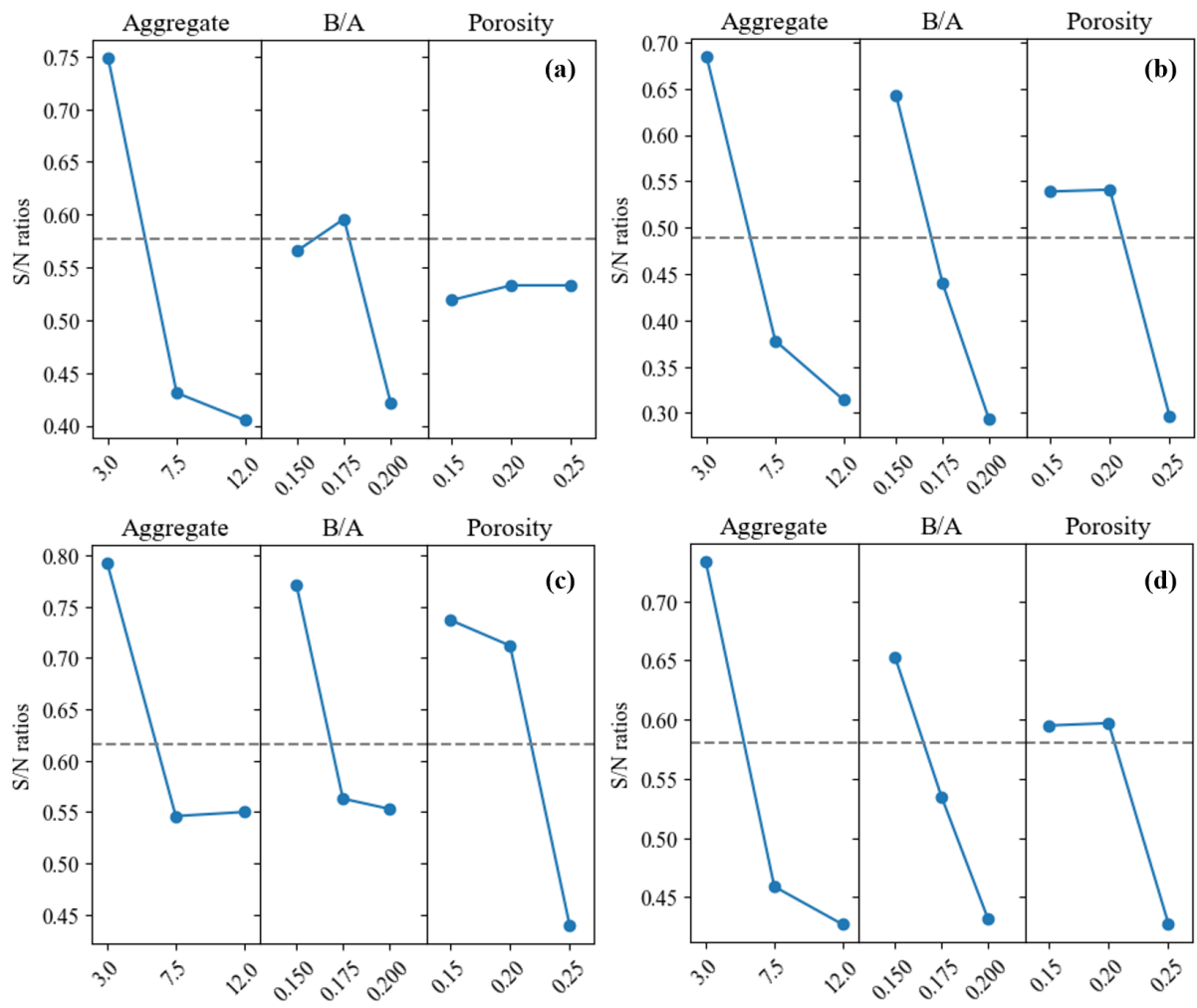
Label	S1	S2	S3	S4
1	0.747	0.913	0.913	0.844
2	0.955	0.872	0.955	0.919
3	0.733	0.470	0.664	0.616
4	0.735	0.809	0.892	0.805
5	0.335	0.191	0.385	0.308
6	0.549	0.514	0.469	0.511
7	0.585	0.603	0.763	0.647
8	0.637	0.633	0.711	0.659
9	0	0	0	0

14

Table 9 Approximation coefficients for Cs adsorption by the four optimization schemes

Label	S1	S2	S3	S4
1	0.603	0.865	0.865	0.760
2	0.864	0.785	0.916	0.848
3	0.778	0.402	0.594	0.591
4	0.606	0.690	0.840	0.707
5	0.330	0.113	0.113	0.202
6	0.358	0.330	0.685	0.469
7	0.490	0.373	0.609	0.491
8	0.595	0.421	0.661	0.556
9	0.130	0.147	0.379	0.235

15



1
2 **Fig. 15** Proximity factors for Sr adsorption under the four optimization schemes: (a) S1, (b) S2, (c) S3, and (d) S4

3 Following Taguchi's optimization process, each performance criterion was subjected to
4 targeted experimental analysis using the signal-to-noise ratio (S/N) to establish the maximum
5 mixing ratios for the three-performance metrics—single-cycle adsorption rate, maximum
6 adsorption capacity, and adsorption efficiency—for Sr and Cs across the four optimization
7 scenarios. For Sr, all four optimization schemes point to an optimal ratio of A1B1C1,
8 corresponding to an aggregate size of 3-6 mm, a B/A ratio of 0.15, and a porosity of 0.15. In
9 contrast, the optimal ratio for Cs varies depending on the performance emphasis: A1B1C1 is
10 optimal when adsorption efficiency is prioritized, while A1B1C2 (aggregate size of 3-6 mm,
11 B/A ratio of 0.15, and a porosity of 0.20) is optimal when maximizing adsorption capacity.
12 When single-cycle adsorption is emphasized, the optimal ratio shifts to A1B2C2, with an
13 aggregate size of 3-6 mm, a B/A ratio of 0.175, and a porosity of 0.20. In the balanced scenario
14 (S4), the optimal ratio is A1B1C2. Overall, the response of the three factors is more pronounced
15 for Cs than for Sr, likely due to Cs's larger ionic radius.

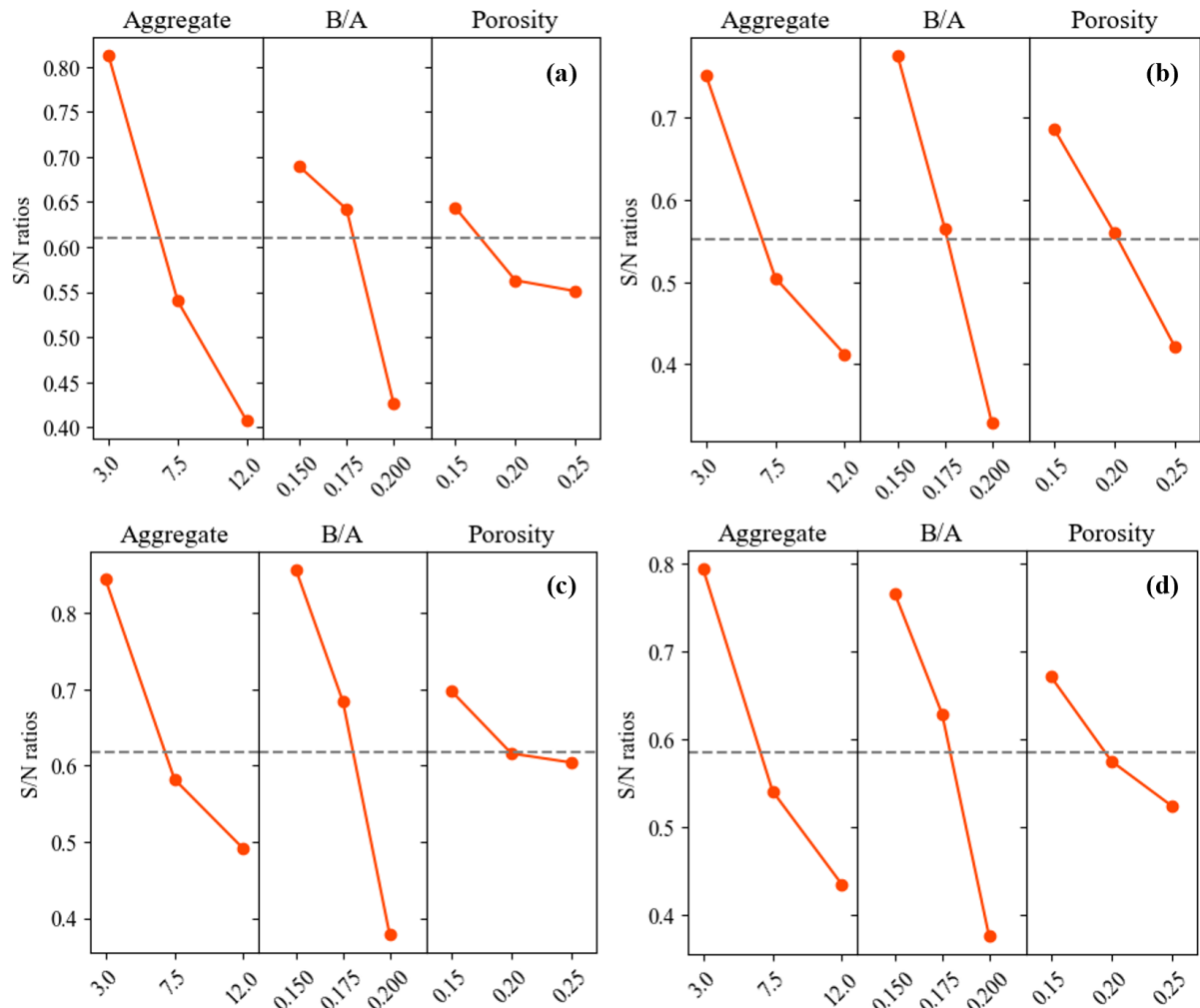


Fig. 16 Proximity factors for Cs adsorption under the four optimization schemes: (a) S1, (b) S2, (c) S3, and (d) S4

Conclusion and future research

The disposal of solid and radioactive waste poses significant risks to earth and marine ecosystems. A proper treatment of such contaminants is not only essential for human welfare and environmental protection, but also promote the recycling of wastes to useful resources. This study addresses these challenges by employing recycled glass (RG) and fly ash (FA) in the development of functional nanocomposite concrete. SEM, TEM and BET analysis revealed a highly porous structure of RrZ powder with mesopores capable to achieve high adsorption efficiency within short time, adhering to quasi-second-order kinetic models. For comparison, the long-term testing showed that FA alone exhibited desorption, whereas when 20% RrZ is mixed with FA, the composite binder maintained stable performance. Moreover, XRD analysis identified key crystalline phases, such as analcime ($\text{NaAlSi}_2\text{O}_6 \cdot \text{H}_2\text{O}$) and low-phase quartz (SiO_4), and no new phases formed after ion exchange with Sr^{2+} and Cs^+ ; while FTIR analysis

1 indicated minimal chemical changes post-adsorption. In addition, the developed PGCC
2 exhibited final adsorption efficiencies ranging from 83.13% to 97.71% for Sr^{2+} and 55.31% to
3 91.01% for Cs^+ , with Sr consistently showing higher adsorption rates. The porosity varying
4 from 14.95% to 25.45% and water permeability from 1.876 to 11.956 mm/s were the key
5 factors for PGCC design, while larger aggregates and lower B/A ratios help optimizing the
6 adsorption. According to ANOVA, aggregate size contributed most significantly to single-
7 cycle adsorption, followed by porosity and B/A ratio.

8
9 Future research should delve deeper into the pore characteristics of PGCC, particularly under
10 the optimal mixing ratios identified in this study. Micron-level CT scanning can provide
11 detailed insights into the pore size distribution and structure of the material, allowing for a
12 more thorough understanding of how these factors influence adsorption performance.
13 Furthermore, to validate the experimental findings, simulations of water seepage and
14 permeability using Ansys Fluent software can provide more accurate predictions of the PGCC
15 composite behavior in real application conditions. Given the potential application of PGCC in
16 marine environment where radionuclide contamination is a significant concern, future research
17 should simulate the performance of PGCC under conditions closer to those found in marine
18 ecosystems. Finally, to ensure the long-term sustainability of PGCC, a comprehensive life
19 cycle assessment (LCA) should be conducted. This will include studying the entire life cycle
20 of PGCC, from material manufacturing to end-of-life disposal and investigating how the
21 material can be recycled or reused after it has reached its full adsorption capacity. This can help
22 to understand the desorption mechanism by developing methods to recover and treat adsorbed
23 radionuclides, and further enhance the material environmental benefits. These findings
24 establish a foundation for further development of geopolymer-based materials for
25 environmental applications, offering a novel approach to managing radioactive waste in a
26 sustainable and scalable manner.

27 **■ Declaration of interests**

28 The authors declare that they have no known competing financial interests or personal
29 relationships that could have appeared to influence the work reported in this paper.

30 **■ Acknowledgements**

31 This work was supported by National Nature Science Foundation of China, Grants No.
32 52108233. Acknowledgements are also given to Bi-carbon Special Program: Science and

1 Technology Special Program for Sustainable Development, Grant No.
2 KCXST20221021111408021, and GJHZ20220913143007013. Acknowledgements is also
3 given to Yudan Lin (Doria) for her help throughout the laboratory testing process.
4

5 ■ References

6 [1] J.P. Absalom, Crout, N. and Young, S.D., Modeling radiocesium fixation in upland
7 organic soils of northwest England, *Environ. Sci. Technol.* 30(9): 2735-2741 (1996).

8 [2] N.e.a. Kinoshita, Assessment of individual radionuclide distributions from the
9 Fukushima nuclear accident covering central-east Japan, *Proc. Natl. Acad. Sci. U.S.A.* 108(49):
10 19526-19529 (2011).

11 [3] Y. Morino, Ohara, T. and Nishizawa, M., Atmospheric behavior, deposition, and
12 budget of radioactive materials from the Fukushima Daiichi nuclear power plant in March 2011,
13 *Geophys. Res. Lett.* 38 L00G11 (2011).

14 [4] S.a.L. Staunton, P., Cs adsorption on the clay-sized fraction of various soils: effect of
15 organic matter destruction and charge compensating cation, *J. Environ. Radioact.* 45(2): 161-
16 172 (1999).

17 [5] K.e.a. Tanaka, Vertical profiles of Iodine-131 and Cesium-137 in soils in Fukushima
18 Prefecture related to the Fukushima Daiichi Nuclear Power Station Accident, *Geochem. J.*
19 46(1): 73 - 76 (2012).

20 [6] N.a.K. Yoshida, J., Tracking the Fukushima radionuclides, *Science* 336(6085): 1115-
21 1116 (2012).

22 [7] M. Gavrilescu, Vasile, P.L., Cretescu, I., Characterization and remediation of soils
23 contaminated with uranium, *J. Hazard Mater.* 163, 475–510 (2009).

24 [8] O.I.M. Ali, Osman, H.H., Sayed, S.A., Shalabi, M.E.H., The removal of some rare
25 earth elements from their aqueous solutions on by-pass cement dust (BCD), *J. Hazard Mater.*
26 195, 62–67 (2011).

27 [9] B.J. Howard, Beresford, N.A., Hove, K., Transfer of radiocaesium to ruminants in
28 natural and semi-natural ecosystems and appropriate counter measures, *Health Phys.* 61, 715–
29 725 (1991).

30 [10] W.W. Cheng, M.; Yang, Z.; Sun, Y.; Ding, C., The efficient enrichment of U(VI) by
31 graphene oxide-supported chitosan, *RSC Adv.* 2014 4 (106), 61919–61926 (2014).

32 [11] Y.Z.Z. Hu, C. F.; Yin, L.; Wen, T.; Yang, Y.; Ai, Y. J.; Wang, X. K., Combining
33 batch technique with theoretical calculation studies to analyze the highly efficient enrichment
34 of U(VI) and Eu(III) on magnetic MnFe₂O₄ nanocubes, *Chem. Eng. J.* 2018, 349, 347–357
35 (2018).

- 1 [12] T.S. Kameda, T.; Yoshioka, T. , Uptake of Nd³⁺ and Sr²⁺ by Li-Al layered double
2 hydroxide intercalated with triethylenetetramine-hexaacetic acid: Kinetic and equilibrium
3 studies, *RSC Adv.* 5 (97), 79447–79455 (2015).
- 4 [13] J. Ma, Wang, C., Xi, W., Zhao, Q., Wang, S., Qiu, M., Wang, J., Wang, X. , Removal
5 of Radionuclides from Aqueous Solution by Manganese Dioxide-Based Nanomaterials and
6 Mechanism Research: A Review, *ACS ES&T Engineering* 1(4), 685–705 (2021).
- 7 [14] J.P.Z. Ma, Q. Y.; Zhou, L. J.; Wen, T.; Wang, J. J. , Mutual effects of U(VI) and
8 Eu(III) immobilization on interpenetrating 3- dimensional MnO₂/graphene oxide composites,
9 *Sci. Total Environ.* 695 (10), 133696 (2019).
- 10 [15] R.D. Ambashta, Sillanpää, M.E.T., Membrane purification in radioactive waste
11 management: a short review, *J. Environ. Radioact.* 105, 76–84 (2012).
- 12 [16] X. Wang, Xu, J., Xu, M., Zhou, B., Liang, J., Zhou, L., High-efficient removal of
13 arsenite by coagulation with titanium xerogel coagulant, *Separ. Purif. Technol.* 258 (2021).
- 14 [17] X. Tang, Zheng, H., Teng, H., Sun, Y., Guo, J., Xie, W., Yang, Q., Chen, W.,
15 Chemical coagulation process for the removal of heavy metals from water: a review, *New Pub:*
16 *Balaban* 57 (4), 1733–1748 (2014).
- 17 [18] M.C. Benalia, Youcef, L., Bouaziz, M.G., Achour, S., Menasra, H., Removal of
18 heavy metals from industrial wastewater by chemical precipitation: mechanisms and sludge
19 characterization, *Arabian J. Sci. Eng.* 47 (5), 5587–5599 (2022).
- 20 [19] Z. Hussain, Sultan, N., Ali, M., Naz, M. Y., AbdEl-Salam, N. M., & Ibrahim, K. A.,
21 Thermochemical Conversion of Waste Glass and Mollusk Shells into an Absorbent Material
22 for Separation of Direct Blue 15 Azo Dye from Industrial Wastewater, *ACS Omega* (2020).
- 23 [20] N.A.A. Qasem, Mohammed, R.H., Lawal, D.U., Removal of heavy metal ions from
24 wastewater: a comprehensive and critical review, *Npj Clean Water* 4 (1), 1–15 (2021).
- 25 [21] A. Dabrowski, Hubicki, Z., Podkořcielny, P., Robens, E., Selective removal of the
26 heavy metal ions from waters and industrial wastewaters by ion-exchange method,
27 *Chemosphere* 56 (2), 91–106 (2004).
- 28 [22] U. Kamran, Rhee, K.Y., Lee, S.Y., Park, S.J., Innovative progress in graphene
29 derivative-based composite hybrid membranes for the removal of contaminants in wastewater:
30 a review, *Chemosphere* 306 (2022).
- 31 [23] A. Mohseni, Kube, M., Fan, L., Roddick, F.A., Treatment of wastewater reverse
32 osmosis concentrate using alginate-immobilised microalgae: integrated impact of solution
33 conditions on algal bead performance, *Chemosphere* 276, 130028 (2021).
- 34 [24] R. Shahrokhi-Shahraki, Benally, C., El-Din, M.G., Park, J., , High efficiency removal
35 of heavy metals using tire-derived activated carbon vs commercial activated carbon: insights
36 into the adsorption mechanisms, *Chemosphere* 264 (2021).

- 1 [25] S.B. Kulkarni, A.; Apte, S. K., Bioprecipitation of uranium from alkaline waste
2 solutions using recombinant deinococcus radiodurans, *J. Hazard. Mater.* 262 (15), 853–861
3 (2013).
- 4 [26] X.L. Zhong, W.; Wang, H. F.; Xue, C.; Hu, B. W. , Aluminum-based metal-organic
5 frameworks (CAU-1) highly efficient UO_2^{2+} and TcO_4^- ions immobilization from aqueous
6 solution., *J. Hazard. Mater.* 407, 124729 (2021).
- 7 [27] X.L.P. Liu, H. W.; Liu, X. W.; Li, Q.; Zhang, N.; Mao, L.; Qiu, M. Q.; Hu, B. W.;
8 Yang, H.; Wang, X. K., Orderly porous covalent organic frameworks-based materials: superior
9 adsorbents for pollutants removal from aqueous solutions, *Innovation* 2 (1), 100076. (2021).
- 10 [28] S.B. D. Das, R. M. R. Dumpala, A. S. Pente, S. Manohar, Separation of radioactive
11 ruthenium from alkaline solution: a solvent extraction and detailed mechanistic approach, *ACS*
12 *Omega* 7, 48, 43803–43812 (2022).
- 13 [29] S.I.S. A. V. Boyarintsev, G. V. Kostikova, V. I. Zhilov, A. M. Safiulina, A.Y.
14 Tsivadze, Separation and purification of elements from alkaline and carbonate nuclear waste
15 solutions, *Nu. Engi. and Tech.* 55, 2, 391-407 (2023).
- 16 [30] C.I. J-B. M. Dassekpo, Z.J. Dong, N.N. Shao, I.S. Dassekpo, D.M. Wang, J.Q. Ye.,
17 Waste glass as a source for green synthesis of mesoporous adsorbent for efficient removal of
18 heavy metals, *Microporous and Mesoporous Materials* 383 (2025) 113393 (2024).
- 19 [31] A. Anderson, Anbarasu, A., Pasupuleti, R.R., Manigandan, S., Praveenkumar, T.R.,
20 Aravind Kumar, J., Treatment of heavy metals containing wastewater using biodegradable
21 adsorbents: a review of mechanism and future trends, *Chemosphere* 295 (2022).
- 22 [32] R. Chakraborty, Asthana, A., Singh, A.K., Jain, B., Susan, A.B.H., Adsorption of
23 heavy metal ions by various low-cost adsorbents: a review, *Int. J. Environ. Anal. Chem.* 102
24 (2), 342–379 (2022).
- 25 [33] M.A. Barakat, New trends in removing heavy metals from industrial wastewater,
26 *Arab. J. Chem.* 4 (4), 361–377 (2011).
- 27 [34] M.S.N. Lisbania V., Edwin E., Marta-Lena A., Farid A., Adsorption of heavy metals
28 on natural zeolites: A review, *Chemosphere* 328 (2023).
- 29 [35] Z.L. Yuxuan J. , Le H. , Yanbo Z. , Li L. , Siyu Z., Zhonghao P., Jiaying L., Dongmin
30 W., Synthesis of coal-analcime composite from coal gangue and its adsorption performance on
31 heavy metal ions,
32 *Journal of Hazardous Materials* 423 (2022) 127027 (2022).
- 33 [36] X. Wang, Wang, X., Pan, S., Yang, Q., Hou, S., Jiao, Y., Zhang, W., Occurrence of
34 analcime in the middle Jurassic coal from the Dongsheng Coalfield, northeastern Ordos Basin,
35 China, *Int. J. Coal Geol.* 196, 126–138 (2018).
- 36 [37] P. Iam-khong, Muchan, P., Sriprang, N., Nithitanakul, M., Synthesis and
37 characterization of a new phase of non Na-loaded analcime zeolite by microemulsion technique,
38 *Solid State Sci.* 96, 105956 (2019).

1 [38] S.N. Azizi, Alavi Daghigh, A., Abrishamkar, M., Phase transformation of zeolite P
2 to Y and analcime zeolites due to changing the time and temperature, *J. Spectrosc.* 2013, 1–5
3 (2013).

4 [39] O.B. Kotova, Shabalin, I.N., Shushkov, D.A., Kocheva, L.S., Hydrothermal synthesis
5 of zeolites from coal fly ash, *Adv. Appl. Ceram.* 115, 152–157 (2016).

6 [40] S.N. Azizi, Daghigh, A.A., Abrishamkar, M., Synthesis of zeolites NaA and analcime
7 using rice husk ash as silica source without using organic template, *J. Mater. Sci.* 45, 5692–
8 5697 (2010).

9 [41] X. Ma, Yang, J., Ma, H., Liu, C., Zhang, P., Synthesis and characterization of
10 analcime using quartz syenite powder by alkali-hydrothermal treatment, *Microporous*
11 *Mesoporous Mater.* 201, 134–140 (2015).

12 [42] Y.-H. Hsiao, Ho, T.-Y., Shen, Y.-H., Ray, D., Synthesis of analcime from sericite
13 and pyrophyllite by microwave-assisted hydrothermal processes, *Appl. Clay Sci.* 143, 378–386
14 (2017).

15 [43] J.H. Taylor, Elmes, V.E., Hurt, A.P., Coleman, N.J., , Synthesis of feldspathoids and
16 zeolite K–F from waste amber container glass, *Mater. Chem. Phys.* 246, 122805 (2020).

17 [44] L.Y. Silpa Kaza, Perinaz Bhada-Tata, and Frank Van Woerden, *What a Waste 2.0,*
18 *A Global Snapshot of Solid Waste Management to 2050,* The World Bank.

19 [45] Z.K. Hussain, A.; Sultan, N.; Ali, M.; Naz, M. Y.; Saed, K.; Sulaiman, S. A. ,
20 Thermo-chemical conversion of waste glass into non vitreous porous material for adsorption
21 application, *J. Mater. Cycles Waste Manage.* 2019, 21, 1132–1143 (2019).

22 [46] U.N.E.P. (UNEP), *Global Waste Management Outlook 2024,* 2024.

23 [47] I. Kheshtzar, Ghorbani, M., Gatabi, M. P., & Lashkenari, M. S., Facile synthesis of
24 smartaminosilane modified-SnO₂/porous silica nanocomposite for high efficiency removal of
25 lead ions and bacterial inactivation, *Journal of Hazardous Materials* 359, 19–30 (2018).

26 [48] R. Dubey, Bajpai, J., & Bajpai, A. K., Green synthesis of graphene sand composite
27 (GSC) as novel adsorbent for efficient removal of Cr (VI) ions from aqueous solution, *Journal*
28 *of Water Process Engineering* 5, 83–94 (2015).

29 [49] S.M. Al-Jubouri, Curry, N. A., & Holmes, S. M., Hierarchical porous structured
30 zeolite composite for removal of ionic contaminants from waste streams and effective
31 encapsulation of hazardous waste, *Journal of Hazardous Materials* 320, 241–251 (2016).

32 [50] J.N. Khaleghi H, Esmaili H, Ramavandi B., Alginate@Fe₃O₄@Bentonite
33 nanocomposite for formaldehyde removal from synthetic and real effluent: optimization by
34 central composite design., *Environ Sci Pollut Res Int.* 30(11): 29566-29580. (2023).

35 [51] G. Crini, Lichtfouse, E., Wilson, L.D., and Morin, N., Conventional and non-
36 conventional adsorbents for wastewater treatment, *Environmental Chemistry Letters* 17,
37 pages195–213 (2019) (2019).

- 1 [52] M.S. Hosseini Hashemi, Eslami, F., and Karimzadeh, R., Organic contaminants
2 removal from industrial wastewater by CTAB treated synthetic zeolite Y, *Journal of*
3 *Environmental Management* 233, PP. 785–792 (2019).
- 4 [53] F.T. Fanta, Dubale, A.A., Bebizuh, D.F., and Atlabachew, M., Copper doped zeolite
5 composite for antimicrobial activity and heavy metal removal from waste water, *BMC*
6 *Chemistry* 13(1), PP 44 (2019).
- 7 [54] C. Söylemez, Türkmen, İ., and Özen, İ., Achieving Dual-Functionality by Surface
8 Coating of Zeolite with Stearic Acid: Combining Breathability and Odor Control Properties in
9 Polyethylene/Zeolite Composite Films, *Macromolecular Research* 28(12), PP.1149–1159
10 (2020).
- 11 [55] N. Keshavarzi, Mashayekhy Rad, F., Mace, A., Ansari, F., Akhtar, F., Nilsson, U.,
12 Berglund, L. and Bergström, L., Nanocellulose–zeolite composite films for odor elimination,
13 *ACS Applied Materials & Interfaces* 7(26), PP.14254-14262 (2015).
- 14 [56] S.A.E. Arent, J. Love, T. Rozsits, B.J. Banka, D. Fisher, D. Ludirdja, G.W.
15 Seegebrecht, W.D. Brant, W. Flood, A. Luke, D. Suchorski, H.J. Brown, B.A. Glaspey, B.
16 Lutey, D.C.T. Tu, J. Casto, L. Haselbach, K.C. Mahboub, C. Tull, M. Chopra, O. Heracklis, A.
17 Marks, R.L. Varner, J. Cook, D.J. Huffman, L.A. Mata, W.J. Weiss, M. Davy, J.T. Kevern, N.
18 Neithalath, K.L. Wolf, J. Norbert, ACI 522 R10 Reported by ACI Committee 522 Report on
19 Pervious Concrete (Reapproved 2011), 2010.
- 20 [57] H.E.-H. F. H. Anwar, M. Hamouda, A. El-Mir, Evaluation of pervious geopolymer
21 concrete pavements performance for effective stormwater infiltration and water purification
22 using Taguchi method, *Materials Today: Proceedings* 90 (2023) 7–11 (2023).
- 23 [58] D. Yan, J. Lu, Y. Sun, T. Wang, T. Meng, Q. Zeng, Y. Liu, CO₂ Pretreatment to
24 Aerated Concrete with High-Volume Industry Wastes Enables a Sustainable Precast Concrete
25 Industry, *ACS Sustainable Chemistry & Engineering* 9(8) (2021) 3363-3375.
- 26 [59] H.W. Wei Huang, Multi-aspect engineering properties and sustainability impacts of
27 geopolymer pervious concrete, *Composites Part B: Engineering* 242 (2022) 110035 (2022).
- 28 [60] P.J. P. Chindapasirt, W. Chalee, U. Rattanasak, Case study of the application of
29 pervious fly ash geopolymer concrete for neutralization of acidic wastewater, *Case Studies in*
30 *Construction Materials* 15 (2021) e00770 (2021).
- 31 [61] Y. Zaetang, Wongsas, A., Sata, V., & Chindapasirt, P., Use of coal ash as geopolymer
32 binder and coarse aggregate in pervious concrete, *Construction and Building Materials* 96,
33 289–295 (2015).
- 34 [62] T. Tho-in, Sata, V., Chindapasirt, P., & Jaturapitakkul, C. , Pervious high-calcium
35 fly ash geopolymer concrete, *Construction and Building Materials* 30, 366–371 (2012).
- 36 [63] Y. Wu, Lu, B., Bai, T., et al., Geopolymer, green alkali activated cementitious
37 material: Synthesis, applications and challenges, *Construction and Building Materials* 224,
38 930–949 (2019).

- 1 [64] A. Mehta, & Siddique, R., Sustainable Geopolymer Concrete using Ground
2 Granulated Blast Furnace Slag and Rice Husk Ash: Strength and Permeability Properties,
3 *Journal of Cleaner Production* 205 (49-57) (2018).
- 4 [65] A.S. A. Azad, S.-F. Mousavi, H. Karami, S. Farzin, V.P. Singh, Effect of zeolite and
5 pumice powders on the environmental and physical characteristics of green concrete filters,
6 *Construction and Building Materials* 240 (2020) 117931 (2020).
- 7 [66] X.L. J. Cheng, Z. Shen, X. Guo, Study on Vegetation Concrete Technology for Slope
8 Protection and Greening Engineering, *Pol. J. Environ. Stud.* 29 (6) (2020) 4017-4028 (2020).
- 9 [67] M.L.H. R.R. Holmes, J.T. Kevern, Enhancing the Ability of Pervious Concrete to
10 Remove Heavy Metals from Stormwater, *J. Sustainable Water Built Environ.* 3(2) (2017)
11 04017004 (2017).
- 12 [68] M.L.H. R.R. Holmes, J.T. Kevern, Removal and Breakthrough of Lead, Cadmium,
13 and Zinc in Permeable Reactive Concrete, *Environmental Engineering Science* 35(5) (2018)
14 408-419 (2018).
- 15 [69] M.S. M. Muthu, M. Kumar, Pb removal in pervious concrete filter: Effects of
16 accelerated carbonation and hydraulic retention time, *Construction and Building Materials* 174
17 (2018) 224-232 (2018).
- 18 [70] L.L.-M. R. Ortega-Villar, C. Coronel-Olivares, L.D. López-León, C.A. Bigurra-
19 Alzati, G.A. Vázquez-Rodríguez, Effect of photocatalytic Fe₂O₃ nanoparticles on urban runoff
20 pollutant removal by permeable concrete, *Journal of Environmental Management* 242 (2019)
21 487-495 (2019).
- 22 [71] M.A.H. M.H. Carr, Artificial Reefs: The Importance of Comparisons with Natural
23 Reefs, *Fisheries* 22(4) (1997) 28-33 (1997).
- 24 [72] M.I.L.-G. L. Carral, J.L.M. Buenhombre, J.J.C. Barros, S. Naya, J. Tarrío-Saavedra,
25 Application of residuals from purification of bivalve molluscs in Galician to facilitate marine
26 ecosystem resiliency through artificial reefs with shells – One generation, *Science of The Total*
27 *Environment* 856 (2023) 159095 (2023).
- 28 [73] K. Collins, Environmental impact assessment of a scrap tyre artificial reef, *ICES*
29 *Journal of Marine Science* 59 (2002) S243-S249 (2015).
- 30 [74] ASTM, ASTM C618-08a, Standard specification for coal fly ash and raw or calcined
31 natural pozzolan for use in concrete, ASTM International 2008.
- 32 [75] JGJ52-2006-Standard for technical requirements and test method of sand and crushed
33 stone (or gravel) for ordinary concrete, 2006.
- 34 [76] Y. Ge, Tang, Q., Cui, X., He, Y., & Zhang, J. , Preparation of large-sized analcime
35 single crystals using the Geopolymer-Gels-Conversion, *Materials Letters* 135, 15–18 (2014).
- 36 [77] L. Itani, Liu, Y., Zhang, W., Bozhilov, K. N., Delmotte, L., & Valtchev, V. ,
37 Investigation of the Physicochemical Changes Preceding Zeolite Nucleation in a Sodium-Rich
38 Aluminosilicate Gel, *Journal of the American Chemical Society* 131(29), 10127–10139 (2009).

- 1 [78] M. Kim, Park, E., & Jurng, J. , Oxidation of gaseous formaldehyde with ozone over
2 MnOx/TiO₂ catalysts at room temperature (25 °C), Powder Technology 325, 368–372 (2018).
- 3 [79] Y. Bu, Chen, Y., Jiang, G., Hou, X., Li, S., & Zhang, Z., Understanding of Au-CeO₂
4 interface and its role in catalytic oxidation of formaldehyde, Applied Catalysis B:
5 Environmental 118138 (2019).
- 6 [80] Q. Qiu, Jiang, X., Lv, G., Chen, Z., Lu, S., Ni, M., J., Yan., Deng, X., Adsorption of
7 heavy metal ions using zeolite materials of municipal solid waste incineration fly ash modified
8 by microwave-assisted hydrothermal treatment, Powder Technology 335, 156–163 (2018).
- 9 [81] R. Ahmad, & Mirza, A., Adsorptive removal of heavy metals and anionic dye from
10 aqueous solution using novel Xanthan gum-Glutathione/Zeolite bionanocomposite,
11 Groundwater for Sustainable Development 7, 305–312 (2018).
- 12 [82] D.P. B. Choudhary, Isotherms, kinetics and thermodynamics of hexavalent
13 chromium removal using biochar, Journal of Environmental Chemical Engineering 6(2) (2018)
14 2335-2343 (2018).
- 15 [83] T.V. Gerasimova, Evdokimova (Galkina), O. L., Kraev, A. S., Ivanov, V. K., &
16 Agafonov, A. V. , Micro-mesoporous anatase TiO₂ nanorods with high specific surface area
17 possessing enhanced adsorption ability and photocatalytic activity, Microporous and
18 Mesoporous Materials 235, 185–194 (2016).
- 19 [84] D.W. O’Connell, Birkinshaw, C., & O’Dwyer, T. F. , Heavy metal adsorbents
20 prepared from the modification of cellulose: A review, Bioresource Technology 99(15), 6709–
21 6724 (2008).
- 22 [85] M.N. El-Sayed, A. A. , Polyethylenimine – functionalized amorphous carbon
23 fabricated from oil palm leaves as a novel adsorbent for Cr(VI) and Pb(II) from aqueous
24 solution, J. Water Process Eng. 2017, 16, 296–308 (2017).
- 25 [86] L.S. P. Castaldi, S. Enzo, P. Melis, Sorption processes and XRD analysis of a natural
26 zeolite exchanged with Pb²⁺, Cd²⁺ and Zn²⁺ cations, Journal of Hazardous Materials 156(1-3)
27 (2008) 428-434 (2008).
- 28 [87] K.T. K. Yoshida, K. Matsunaga, A. Nakahira, H. Kurata, Y.H. Ikuhara, Y. Sasaki,
29 Atomic sites and stability of Cs⁺ captured within zeolitic nanocavities, Scientific Reports 3(1)
30 (2013) 2457 (2013).
- 31 [88] K.S. Q. Tian, Structural characterizations of fly ash-based geopolymer after
32 adsorption of various metal ions, Environmental Technology 42(6) (2021) 941-951 (2021).
- 33 [89] K.L. L. Price, A. Sartbaeva, Local and Average Structural Changes in Zeolite A upon
34 Ion Exchange, Magnetochemistry 3(4) (2017) 42 3(4) (2017) 42. (2017).
- 35 [90] K.P. C.E. White, N.J. Henson, J.L. Provis, In situ synchrotron X-ray pair distribution
36 function analysis of the early stages of gel formation in metakaolin-based geopolymers,
37 Applied Clay Science 73 (2013) 17-25 (2013).

- 1 [91] J.L.P. C.E. White, A. Llobet, T. Proffen, J.S.J. Van Deventer, Evolution of Local
2 Structure in Geopolymer Gels: An *In Situ* Neutron Pair Distribution Function Analysis,
3 Journal of the American Ceramic Society 94(10) (2011) 3532-3539 (2011).
- 4 [92] C.E.W. M.E. Natali, M.C. Bignozzi, Elucidating the atomic structures of different
5 sources of fly ash using X-ray and neutron PDF analysis, Fuel 177 (2016) 148-156 (2016).
- 6 [93] C.A. Rees, J.L. Provis, G.C. Lukey, J.S.J. van Deventer, In situ ATR-FTIR study of
7 the early stages of fly ash geopolymer gel formation, Langmuir 23(17) (2007) 9076-9082.
- 8 [94] W.M. M. Król, K. Barczyk, T. Bajda, M. Kozanecki, Changes in the Vibrational
9 Spectra of Zeolites Due to Sorption of Heavy Metal Cations, J Appl Spectrosc. 80(5) (2013)
10 644-650 (2013).
- 11 [95] K.S. Q. Tian, Application of fly ash-based materials for stabilization/solidification of
12 cesium and strontium, Environ Sci Pollut Res. 26(23) (2019) 23542-23554 (2019).
- 13 [96] M.A.L.-M. J.L. Valentín, A. Rodríguez, P. Posadas, L. Ibarra, Novel anhydrous
14 unfolded structure by heating of acid pre-treated sepiolite, Applied Clay Science 36(4) (2007)
15 245-255 (2007).
- 16 [97] C.N. G. Coudurier, J.C. Vedrine, Uses of I.R. spectroscopy in identifying ZSM
17 zeolite structure, J. Chem. Soc., Chem. Commun. (24) (1982) 1413-1415 (1982).
- 18 [98] M.A. E. Koohsaryan, Nanosized and hierarchical zeolites: A short review, Chinese
19 Journal of Catalysis 37(4) (2016) 447-467 (2016).
- 20
- 21

Supplementary Materials

Performance and characterization of nano-engineered silica waste concrete composite for efficient marine radionuclides remediation

Jean-Baptiste Mawulé Dassekpo^{a,*}, Chonkei Iong^b, Dejing Chen^b,
Feng-liang Zhang^b, Xiaoxiong Zha^b, Jianqiao Ye^{c,*}

^a Institute of Technology for Marine Civil Engineering, Shenzhen Institute of Information Technology, 518172, PR. China

^b School of Civil and Environmental Engineering, Harbin Institute of Technology, Shenzhen, 518055, China

^c School of Engineering, Lancaster University, Lancaster LA1 4YR, UK

*Corresponding authors email: dassekpo.jb@szit.edu.cn, j.ye2@lancaster.ac.uk

1.1 Porosity and permeability coefficient measurement

The porosity and permeability coefficients of the produced GPCC were also measured. For the porosity test, the samples were baked at 105°C until they reached constant weights, which, in this case, took 24 h. Once removed from the oven, the samples were placed in a desiccator to cool under ambient conditions. The dimensions of the samples were then measured using a straightedge, and their volumes were calculated accordingly. Next, the samples were fully submerged in water, and their weights were measured using a hydrostatic scale once no air bubbles appeared on the surface. After soaking, the samples were removed from the water, placed in a temperature-controlled oven, and heated at 60°C for 24 h. Following this heating period, the samples' weights were measured again and recorded. Finally, the porosity of the samples was determined in accordance with the DB11/T 775–2010 standard [1] using the following equation:

$$v = \left[1 - \frac{m_2 - m_1}{\rho V} \right] \times 100\% \quad (4)$$

1
2
3
4
5
6
7
8
9
10
11
12
13
14
15
16
17
18
19
20
21
22
23
24

Where: v is the porosity (%); m_1 , the weight of the sample in water (g); m^2 , the weight of the sample after baking in the oven for 24 h (g); ρ , the density of water (g/cm^3); and V , the volume of the sample (cm^3).

After confirming the porosity of PGCC, the permeability of cubic samples was measured. The sample was wrapped in sealing film and mounted at an appropriate height within the device's square side frame. The edges were then sealed with waterproof sealant at the contact area between the sample and the storage square tube, as shown in Fig. 3(d). Once the sample was fixed and the device filled with water, the permeability test began after the water flow reached a steady state. The procedure was as follows: (1) Measure the surface area (A) and thickness (D) of the sample using Vernier calipers; (2) Mount the sample in the vertical frame of the testing system; (3) Seal the sample's perimeter with waterproof material to ensure water tightness, allowing water penetration only through the lower and upper surfaces of the sample; (4) Set the vacuum pump to 90 kPa and maintain it for 30 min, while watering, cover the sample, ensuring a water level about 10 cm above the sample surface; (5) Stop the vacuum, immerse the sample for 20 min, then transfer it to the constant head water permeability test system, as shown in Fig. 3(a), and firmly seal the sample within the device; (6) Open the water supply valve to fill the overflow tank, allowing water to exit through the overflow hole. Adjust the water flow so that the sample maintains a water level of about 150 mm. Measure the water level difference (H) between the sample surface and the overflow tank using a steel ruler, (7) After the water begins to overflow from the sample, collect the outflow in a dry container for 5 min and record the volume; (8) Once the overflow from the sample and tank stabilizes, collect water from the outlet in a dry container, record the outflow for 5 min, weigh the water with an electronic scale, and calculate the water volume (V) using the density value from Table 2. (9)

1 Repeat step 8 after the overflow stabilizes again; (10) Measure the temperature (T) of the water
2 in the overflow tank during the test using a precision thermometer.

3 The water permeability coefficient (k) was the average of three samples and calculated
4 according to Darcy's law by the following equation:

$$5 \quad k_T = \frac{QL}{HAt} \quad (5)$$

6

7 Where: k is the water permeability coefficient of the sample when the water temperature is
8 T°C, in millimeters per second (mm/s); Q, the amount of water collected in time t in second
9 (mm³/s); L, the thickness of the sample (mm); H, the head of the water reflecting the difference
10 in water level (mm); A, the cross-section surface of the sample (mm²); and t the time (s).

11

$$12 \quad k_{15} = k_T \frac{\eta_T}{\eta_{15}} \quad (6)$$

13

14 Where: k_T is the water permeability coefficient of the sample at the standard temperature
15 (mm/s); η_T, the kinetic viscosity coefficient of water at T°C (kPa.s); η₁₅, the kinetic viscosity
16 coefficient of water at 15°C (kPa.s); η_T/η₁₅ designs the ratio of kinetic viscosity coefficient of
17 water. The dynamic viscous coefficient ratio of water is referred to JC/T 2558-2020 standard
18 [2].

19

20 **1.2 Pair distribution function (PDF)**

21 Furthermore, the pair distribution function (PDF) has proven to be an effective technique
22 for uncovering the local atomic structure of complex materials, including disordered substances
23 [3, 4]. The reduced PDF, G(r), is obtained from the Fourier sine transform of the reduced
24 structure function, F(Q) = Q[S(Q) - 1], as illustrated in Eq. (10). Here, Q is defined in Eq. (11),

1 θ represents the scattering angle, and λ is the wavelength of the light source. Total scattering
2 data were collected using a Bruker D8 unit with Mo K α radiation as the X-ray source, yielding
3 a wavelength of 0.7107 Å and a Q value of 17.5 Å. Powder X-ray diffraction patterns were
4 recorded over an angular range of 5° to 130°, at a scanning speed of 2° per minute and a step
5 size of 0.02°, with a total recording time of 5 hours. PDFs were processed using PDFgetX3 [5],
6 following standard data processing procedures.

$$7 \quad G(r) = \frac{2}{\pi} \int_0^{\infty} Q[S(Q) - 1] \sin(Qr) dQ \quad (10)$$

$$8 \quad Q = \frac{4\pi \sin \theta}{\lambda} \quad (11)$$

9

10 **1.3 Taguchi Analysis**

11 The Taguchi method uses an orthogonal array-based on Gaussian quadratic functions to
12 limit the number of experiments [6, 7]. The method entails evaluating the desired attributes by
13 considering relevant factors and their corresponding levels, then assessing them using the
14 signal-to-noise (S/N) ratio [8]. Optimization is necessary when there is a discrepancy between
15 the expected and obtained responses. The values and noise figures align with the desired
16 outcomes. The S/N values are calculated based on the optimization characteristics of the target
17 parameter (response), following the principles of "bigger is better," "smaller is better," and
18 "nominal is better," as illustrated in the respective Eqs. (12-14)." Larger is better" indicates
19 response maximization, while "smaller is better" indicates response minimization. The analysis
20 in this paper uses the results obtained from the 9 experimental mixtures for the considered
21 properties. For all the properties, i.e., single-cycle adsorption efficiency and maximum
22 adsorption rate, a signal-to-noise ratio of "bigger is better" was chosen as these properties
23 should be maximized in porous or permeable concrete applications, while a signal-to-noise
24 ratio of "smaller is better" was chosen for adsorption efficiency.

1

2 $S/N_S = -10 \times \log_{10} \left(\frac{1}{n} \sum_{i=1}^n Y_i^2 \right) \rightarrow$ Smaller is better (12)

3 $S/N_L = -10 \times \log_{10} \left(\frac{1}{n} \sum_{i=1}^n \frac{1}{Y_i^2} \right) \rightarrow$ Larger is better (13)

4 $S/N_N = -10 \times \log_{10} \left(\frac{1}{n} \sum_{i=1}^n (Y_i - Y_o)^2 \right) \rightarrow$ Nominal is better (14)

5

6 **References**

7 [1] DB11/T 775 - 2010 Technical specification for pervious concrete
8 pavement, 2010.

9 [2] JC/T2558-2020 Pervious concrete specification, performance
10 indicators and testing analysis, 2020.

11 [3] P.S. J.L. Bell, J.L. Provis, R.P. Haggerty, P.E. Driemeyer, P.J.
12 Chupas, J.S.J. Van Deventer, W.M. Kriven, Atomic Structure of a Cesium
13 Aluminosilicate Geopolymer: A Pair Distribution Function Study, Chem. Mater.
14 20(14) (2008) 4768-4776 (2008).

15 [4] J.L.P. C.E. White, T. Proffen, J.S.J. Van Deventer, The Effects of
16 Temperature on the Local Structure of Metakaolin -Based Geopolymer Binder:
17 A Neutron Pair Distribution Function Investigation, Journal of the American
18 Ceramic Society 93(10) (2010) 3486-3492 (2010).

19 [5] T.D. P. Juhas, C.L. Farrow, S.J.L. Billinge, PDFgetX3: A rapid and
20 highly automatable program for processing powder diffraction data into total
21 scattering pair distribution functions, J Appl Crystallogr. 46(2) (2013) 560-
22 566 (2013).

23 [6] T.J. C. Chen, Y. Zhuang, X. Lin, Workability, mechanical properties
24 and affinity of artificial reef concrete, Construction and Building Materials
25 98 (2015) 227-236 (2015).

1 [7] C.N. G. Coudurier, J.C. Vedrine, Uses of I.R. spectroscopy in
2 identifying ZSM zeolite structure, J. Chem. Soc., Chem. Commun. (24) (1982)
3 1413-1415 (1982).

4 [8] K. Collins, Environmental impact assessment of a scrap tyre
5 artificial reef, ICES Journal of Marine Science 59 (2002) S243-S249 (2015).

6

7